

TTK-10-29
 SFB/CPP-10-26
 April 13, 2010

Electroweak non-resonant NLO corrections to $e^+e^- \rightarrow W^+W^-b\bar{b}$ in the $t\bar{t}$ resonance region

M. BENEKE, B. JANTZEN and P. RUIZ-FEMENÍA

*Institut für Theoretische Teilchenphysik und Kosmologie,
 RWTH Aachen University,
 D – 52056 Aachen, Germany*

Abstract

We analyse subleading electroweak effects in the top anti-top resonance production region in e^+e^- collisions which arise due to the decay of the top and anti-top quarks into the $W^+W^-b\bar{b}$ final state. These are NLO corrections adopting the non-relativistic power counting $v \sim \alpha_s \sim \sqrt{\alpha_{EW}}$. In contrast to the QCD corrections which have been calculated (almost) up to NNNLO, the parametrically larger NLO electroweak contributions have not been completely known so far, but are mandatory for the required accuracy at a future linear collider. The missing parts of these NLO contributions arise from matching coefficients of non-resonant production-decay operators in unstable-particle effective theory which correspond to off-shell top production and decay and other non-resonant irreducible background processes to $t\bar{t}$ production. We consider the total cross section of the $e^+e^- \rightarrow W^+W^-b\bar{b}$ process and additionally implement cuts on the invariant masses of the W^+b and $W^-\bar{b}$ pairs.

1 Introduction

The top quark is currently known from direct production at the Fermilab Tevatron to weigh $m_t = 173.1 \pm 0.6$ (stat.) ± 1.1 (syst.) GeV [1], and an increase in precision to about 1 GeV is expected soon from the Large Hadron Collider (LHC). From a threshold scan of the $e^+e^- \rightarrow t\bar{t}$ cross section at the planned International Linear Collider (ILC), however, a precision of 30 MeV can be achieved experimentally [2]. Aside from determining a fundamental parameter of the Standard Model, accurate top-mass measurements constrain the quantum fluctuations from non-standard interactions in electroweak precision measurements. Other characteristics of the top quark such as its width and Yukawa coupling provide information about its coupling to other particles and the mechanism of electroweak symmetry breaking. For these reasons (and perhaps also because it represents the cleanest non-relativistic system bound by the colour force) top-quark pair production near threshold in e^+e^- annihilation has been thoroughly investigated following the non-relativistic approach of [3,4,5], which treats the leading colour-Coulomb force exactly to all orders in perturbation theory. In this framework, where the strong coupling α_s is of the same order as v , the small relative velocity of the top and anti-top, next-to-next-to-leading order (NNLO) corrections have been available for some time [6,7,8,9,10,11,12], next-to-leading and some higher-order logarithms of v have been summed to all orders [13,14,15,16], and the third-order (NNNLO) cross section is now known almost completely [17,18,19], which requires input from three-loop matching coefficients [20], potentials [21,22,23,24,25], and third-order S-wave energy levels and residues [17,26,27,28]. The full NNNLO result should finally clarify the question whether the QCD corrections can be calculated with the required precision.

Here we focus on a different issue, non-resonant production of the physical final state after top decay, which though known for some time (see, e.g., the discussion in [29]) has been left aside up to now. The top quark is unstable with a significant width Γ_t of about 1.5 GeV due to the electroweak interaction. The width is essential in threshold production, since it prevents the top and anti-top from forming a bound state [30] and causes a broad resonance structure in the energy dependence of the cross section on top of the increase due to the opening-up of the two-particle phase space. However, once the top width is included, due to top decay, the physical final state is $W^+W^-\bar{b}\bar{b}$ – at least if we neglect the decay of top into strange and down quarks, as justified by $V_{tb} \approx 1$, and consider W bosons as stable, which we may assume for the purpose of discussion in the present paper. The $W^+W^-\bar{b}\bar{b}$ final state can be reached through non-resonant top production or background processes containing no or only single top quarks. Both effects are not included in the non-relativistic treatment. Adopting a standard counting scheme where $\alpha_{EW} \sim \alpha_s^2$, we find that the leading non-resonant and off-shell effects are next-to-leading order (NLO) for the total cross section, since there is an additional power of α_{EW} but no phase-space suppression, hence the relative correction is $\alpha_{EW}/v \sim \alpha_s$. We note that some of the higher-order NNLO corrections due to the finite top width have already been calculated in [31].

In this paper we calculate the complete NLO “electroweak” contributions to the

$e^+e^- \rightarrow W^+W^-b\bar{b}$ process in the $t\bar{t}$ resonance region, for the total cross section as well as including invariant-mass cuts on the Wb pairs. The calculation is performed with unstable-particle effective field theory [32,33], which provides the framework for consistently including resonant and non-resonant effects while maintaining an expansion in the small parameters of the problem. There are many similarities with W -pair production considered in [34,35], though the top-quark case is technically more complicated due to the presence of a massive particle (the W boson) in top decay. We note that an alternative approach has been developed in parallel [36,37] that includes the effects of invariant-mass cuts on the Wb pairs entirely through calculations in non-relativistic effective theory. This works if the invariant-mass cuts around m_t are neither very loose nor very tight, and provided that the non-resonant background processes are small, which must be checked by other means. The present approach removes both these restrictions and can be used in particular for the total cross section. We shall see that when both approaches are applicable, they agree well for top-quark production.

There is an interesting conceptual issue concerning the pure QCD calculation of the $t\bar{t}$ cross section. It exhibits an uncanceled ultraviolet divergence (here regularized dimensionally)

$$\sigma_{t\bar{t}} \propto \frac{\alpha_s \Gamma_t}{\epsilon} \propto \frac{\alpha_s \alpha_{\text{EW}}}{\epsilon} \quad (1)$$

at NNLO, which arises from the logarithmic overall divergence in the two-loop non-relativistic correlation function, whose imaginary part gives the cross section. The overall divergence is polynomial in the non-relativistic energy E of the top quarks, but contributes to the cross section, since the correlation function is evaluated at complex values $E \rightarrow E + i\Gamma_t$. As discussed in [19] this divergence cancels with an infrared divergence that appears in the non-resonant term in unstable-particle effective theory from the diagram corresponding to off-shell top-quark decay. The lesson from this is that the pure QCD result alone that is usually shown in the literature is inconsistent theoretically and must be embedded in the systematic calculation of the $e^+e^- \rightarrow W^+W^-b\bar{b}$ process. In the present paper, however, we are concerned with NLO accuracy, where no explicit divergence arises in dimensional regularization. But the problem at NLO is in fact worse. Inspection of the one-loop non-relativistic correlation function shows that it is linearly ultraviolet divergent, or more generally exhibits a cut-off dependence of the NLO order, just as the non-resonant contribution that we calculate below has a linear infrared divergence. Both require regularization and as usual dimensional regularization yields finite (but regularization-dependent) values in four dimensions for linearly divergent integrals. The conclusion is that the non-resonant NLO contribution that we consider here is mandatory to obtain a regularization-independent result for top anti-top production, more precisely $W^+W^-b\bar{b}$ production in the $t\bar{t}$ threshold region, at NLO.

The outline of the paper is as follows. In Section 2 we briefly review unstable-particle effective theory. We list the terms that contribute at NLO to the $e^+e^- \rightarrow W^+W^-b\bar{b}$ process, when counting $\alpha_s \sim \sqrt{\alpha_{\text{EW}}} \sim v$, and explain that the non-resonant electroweak contribution is obtained from the $e^+e^- \rightarrow t W^- \bar{b}$ amplitude and its charge-conjugate with the top-quark width set to zero. The computation is described and

the results are summarized in Section 3 and Appendix A. In Section 4 we discuss the implementation of invariant-mass cuts in the effective-theory calculation and validate our result by comparing it to the Born cross section for the $e^+e^- \rightarrow W^+W^-b\bar{b}$ process computed numerically with MadGraph/MadEvent. Finally, in Section 5 we combine the new non-resonant contributions with the resummed leading-order QCD result and the electromagnetic correction due to the electromagnetic Coulomb potential, which constitutes another electroweak NLO effect, and discuss the top anti-top line-shape as seen in the energy-dependence of the physical $W^+W^-b\bar{b}$ final state compared to the pure QCD calculation of $t\bar{t}$ production. We conclude in Section 6.

2 Method of calculation

2.1 Unstable-particle effective theory for pair production near threshold

The cross section for the $e^+e^- \rightarrow W^+W^-b\bar{b}$ process (inclusive but also in the case where we allow for cuts in the invariant masses of the W^+b and $W^-\bar{b}$ subsystems) is obtained from the $W^+bW^-\bar{b}$ cuts of the e^+e^- forward-scattering amplitude. In the energy region $\sqrt{s} \approx 2m_t$ close to the top anti-top production threshold, the amplitude is dominated by the production of resonant top quarks with small virtuality. This allows us to integrate out hard modes with scale m_t and represent the forward-scattering amplitude as the sum of two terms [32,33],

$$i\mathcal{A} = \sum_{k,l} C_p^{(k)} C_p^{(l)} \int d^4x \langle e^-e^+ | T[i\mathcal{O}_p^{(k)\dagger}(0) i\mathcal{O}_p^{(l)}(x)] | e^-e^+ \rangle + \sum_k C_{4e}^{(k)} \langle e^-e^+ | i\mathcal{O}_{4e}^{(k)}(0) | e^-e^+ \rangle. \quad (2)$$

In the subsequent discussion of top-quark pair production near threshold we follow closely the formalism described in [34] for four-fermion production in e^+e^- collisions in the energy region of the W -pair production threshold, and refer to that paper for further details on the method.

The matrix elements in (2) are evaluated in the “low-energy” effective theory, which includes elements of soft-collinear and non-relativistic effective theory. The first term on the right-hand side of (2) describes the production of a resonant $t\bar{t}$ pair in terms of production (decay) operators $\mathcal{O}_p^{(l)}(x)$ ($\mathcal{O}_p^{(k)\dagger}(x)$) with short-distance coefficients $C_p^{(k,l)}$. The second term accounts for the remaining non-resonant contributions. Note that there is no separate term for the production of one resonant and one off-shell top [34,37], since such configurations are not sensitive to the particular low-energy dynamics that develops at the pair-production threshold. They are effectively short-distance and included in the coefficient functions $C_{4e}^{(k)}$ of non-resonant production-decay operators $\mathcal{O}_{4e}^{(k)}(0)$.

The standard pure QCD calculation of top-pair production near threshold is entirely contained in the resonant term. In this paper we are mainly concerned with the calculation of the leading contribution to $C_{4e}^{(k)}$, which represents an NLO correction to the forward-scattering amplitude \mathcal{A} , since the first term in (2) is of order $\alpha_{\text{EW}}^2 v$, while the second is $\mathcal{O}(\alpha_{\text{EW}}^3)$. Nevertheless, for comparison and to discuss other NLO non-QCD effects, we briefly summarize the expressions relevant to the leading-order resonant term. There are only two production operators at this order,

$$\mathcal{O}_p^{(v)} = \bar{e}_{c_2} \gamma_i e_{c_1} \psi_t^\dagger \sigma^i \chi_t, \quad \mathcal{O}_p^{(a)} = \bar{e}_{c_2} \gamma_i \gamma_5 e_{c_1} \psi_t^\dagger \sigma^i \chi_t, \quad (3)$$

where ψ_t (χ_t) denotes the non-relativistic top (anti-top) field, e_c a collinear electron field with large, light-like momentum in a direction labelled by c , and $\gamma_i = -\gamma^i$. We drop the Wilson lines required to make the operators gauge-invariant, since they do not contribute to our calculation. The tree-level coefficient functions of these operators are computed from the tree-level amplitude of the process $e^+ e^- \rightarrow t\bar{t}$ at production threshold $\sqrt{s} = 2m_t$ and are given by (keeping the full s -dependence in the photon and Z propagators)

$$\begin{aligned} C_p^{(v)} &= 4\pi\alpha \left[\frac{Q_t Q_e}{s} + \frac{v_e v_t}{s - M_Z^2} \right], \\ C_p^{(a)} &= -4\pi\alpha \frac{a_e v_t}{s - M_Z^2}, \end{aligned} \quad (4)$$

where α denotes the electromagnetic coupling, Q_f the electric charge of fermion species f in units of the positron charge ($Q_t = 2/3$, $Q_e = -1$), and M_Z the Z -boson mass. The vector and axial-vector coupling of the fermion f to the Z -boson are given by

$$v_f = \frac{T_3^f - 2Q_f s_w^2}{2s_w c_w}, \quad a_f = \frac{T_3^f}{2s_w c_w}, \quad (5)$$

where s_w (c_w) is the sine (cosine) of the weak mixing angle and T_3^f the third component of the weak isospin of the fermion. In terms of these quantities the leading-order cross section is given by

$$\sigma_{t\bar{t}}^{(0)} = \frac{1}{s} \text{Im} \mathcal{A}^{(0)} = \left[C_p^{(v)2} + C_p^{(a)2} \right] 2N_c \text{Im} G_C^{(0)}(0, 0; \mathcal{E}), \quad (6)$$

where $E \equiv \sqrt{s} - 2m_t$ and $\mathcal{E} \equiv E + i\Gamma_t$, $N_c = 3$ equals the number of colours, and $G_C^{(0)}(0, 0; \mathcal{E})$ denotes the $\overline{\text{MS}}$ -renormalized zero-distance Coulomb Green function [38]

$$\begin{aligned} G_C^{(0)}(0, 0; \mathcal{E}) &= -\frac{m_t^2}{4\pi} \left\{ \sqrt{-\frac{\mathcal{E}}{m_t}} + \alpha_s C_F \left[\frac{1}{2} \ln \left(-\frac{4m_t \mathcal{E}}{\mu^2} \right) - \frac{1}{2} \right. \right. \\ &\quad \left. \left. + \gamma_E + \psi \left(1 - \frac{\alpha_s C_F}{2\sqrt{-\mathcal{E}/m_t}} \right) \right] \right\}. \end{aligned} \quad (7)$$

Here γ_E is the Euler-Mascheroni constant, μ the scale introduced in dimensional regularization, and ψ the Euler psi-function. (The dependence on μ and the regularization drops out in $\text{Im } G_C^{(0)}(0, 0; \mathcal{E})$.)

The leading contribution from non-resonant production-decay operators $\mathcal{O}_{4e}^{(k)}$ to (2) arises from four-electron operators of the form

$$\mathcal{O}_{4e}^{(k)} = \bar{e}_{c_1} \Gamma_1 e_{c_2} \bar{e}_{c_2} \Gamma_2 e_{c_1}, \quad (8)$$

where Γ_1, Γ_2 are Dirac matrices. The calculation of the short-distance coefficients $C_{4e}^{(k)}$ is performed in standard fixed-order perturbation theory in the full electroweak theory. In particular, the top propagator is the free propagator not including the top width, which ensures that the amplitude depends only on the short-distance scales. Self-energy insertions are treated perturbatively and are not resummed into the propagators. The leading contribution to the forward-scattering amplitude arises from the one-loop diagrams with two top propagators. Just as in the case of W -boson pair production [34] the imaginary part of these diagrams vanishes in dimensional regularization to all orders in the expansion in $E = \sqrt{s} - 2m_t$ in the hard region. Thus the leading imaginary parts of $C_{4e}^{(k)}$ arise from two-loop diagrams of order α_{EW}^3 shown in Figure 1 below. The corresponding contribution to the cross section is

$$\sigma_{\text{non-res}} = \frac{1}{s} \sum_k \text{Im} \left[C_{4e}^{(k)} \right] \langle e^- e^+ | i \mathcal{O}_{4e}^{(k)}(0) | e^- e^+ \rangle. \quad (9)$$

It is convenient not to calculate the $C_{4e}^{(k)}$ separately, but directly the sum (9) when one considers the unpolarized cross section. Technically, this simply amounts to the calculation of the spin-averaged tree-level processes $e^+ e^- \rightarrow tW^- \bar{b}$ and $e^+ e^- \rightarrow \bar{t}W^+ b$ with no width supplied to the intermediate top-quark propagators. Instead, the divergence from the top-quark propagators going on-shell is regularized dimensionally.

2.2 NLO corrections related to the top-quark instability and electroweak interactions

In the following we list the NLO corrections to the $e^+ e^- \rightarrow W^+ W^- b \bar{b}$ process in the top anti-top resonance region $\sqrt{s} \approx 2m_t$. We do not discuss in this paper the pure QCD NLO corrections consisting of the one-loop QCD correction to the $\gamma^*(Z) t \bar{t}$ vertex and the one-loop correction to the QCD Coulomb potential, since they are standard and included in the pure QCD calculations in the literature. Instead we focus on NLO corrections which arise once we consider the $W^+ W^- b \bar{b}$ final state (as required by the top instability), and other electroweak effects:

- The single insertion of the (leading-order) electromagnetic Coulomb interaction instead of the colour Coulomb interaction is an NLO effect, since $\alpha/\alpha_s \sim \alpha_s$. This is trivially accounted for, including some higher-order terms, by replacing $\alpha_s C_F \rightarrow \alpha_s C_F + \alpha Q_t^2$ in (7). This effect has already been studied in [16,37].

- The one-loop QCD correction to the on-shell top width [39] is also trivially included by using the one-loop corrected expression for Γ_t in the variable $\mathcal{E} \equiv E + i\Gamma_t$ in (7). We do not discuss this effect further in this paper, however, since in the pure QCD calculation the top width is considered as an adjustable input parameter, and thus may be thought of as representing the one-loop corrected expression.
- Corrections coming from gluon exchange involving the bottom quarks in the final state (QCD interference effects) appear at NLO but vanish at NLO for the total cross section [40]. We show in Section 4 that they are parametrically suppressed in the presence of invariant-mass cuts, provided the cuts are loose in the sense defined below (see also [37]). Since we focus on loose cuts in the final results, no calculation of interference effects is required.
- Non-resonant contributions start at NLO, as discussed above. They arise from the hard contributions to the Born cross section for $e^+e^- \rightarrow W^+W^-b\bar{b}$, which determine the matching coefficients of the four-electron production-decay operators. We calculate this contribution in Section 3.

We should note that any three-particle final state produced through the electroweak interaction in e^+e^- annihilation contributes at NLO (namely $\mathcal{O}(\alpha_{\text{EW}}^3)$) provided the $W^+W^-b\bar{b}$ final state can be reached through the resonant decay of one of the three particles with a significant branching fraction of the decaying resonance. The obvious relevant cases are $tW^-\bar{b}$ and $\bar{t}W^+b$ considered in Section 3; others are $e^+e^- \rightarrow W^+W^-H$ for low Higgs masses, when $H \rightarrow b\bar{b}$ is the dominant decay mode, and $e^+e^- \rightarrow Hb\bar{b}$, when the Higgs decays resonantly to W^+W^- with a large branching fraction. The process $e^+e^- \rightarrow W^+W^-Z$ with Z decaying to $b\bar{b}$ is less prominent, since the $Z \rightarrow b\bar{b}$ branching fraction is only about 15%. We do not compute these additional three-particle processes in the present paper, since they are further suppressed when invariant-mass cuts in the top anti-top signal region are applied. Moreover, in a realistic analysis these contributions would be eliminated anyway by invariant-mass cuts on the resonance (Higgs or Z) decay products.

3 Computation of the four-electron matching coefficients at NLO

The four-electron matching coefficients $C_{4e}^{(k)}$ originate from the hard contributions of the e^+e^- forward-scattering amplitude. The hard momentum region expansion dictates that the top-quark self-energy insertions are treated perturbatively, since the top lines are formally far off-shell, $p_t^2 - m_t^2 \sim \mathcal{O}(m_t^2) \gg \Sigma(p_t^2)$. Accordingly the calculation of the coefficients $C_{4e}^{(k)}$ is performed in fixed-order perturbation theory in the full electroweak theory with no resummation of self-energy insertions in the top-quark propagator [34] and supplemented with an expansion of the amplitudes in $\delta = s/(4m_t^2) - 1 \sim v^2$. The corresponding contributions to the imaginary part of the forward-scattering amplitude

are then reproduced by those imaginary parts of the short-distance coefficients $C_{4e}^{(k)}$ which can be identified with the $W^+W^-b\bar{b}$ final state. The extraction of these imaginary parts is more conveniently performed by evaluating the relevant cuts of the hard e^+e^- forward-scattering diagrams directly. The leading contribution arises from the cut one-loop diagram with a top and anti-top propagator; however, the hard region of this diagram vanishes in dimensional regularization to all orders in the δ -expansion.

A non-zero imaginary contribution to the short-distance coefficients $C_{4e}^{(k)}$ arises, in the unitary gauge, from the cut two-loop diagrams shown in Figure 1 expanded near threshold (in $\delta = s/(4m_t^2) - 1$). Including cuts of the top lines is consistent with the expansion of the imaginary part of the resummed top-quark propagator in the hard region [34]¹. The contribution to the $W^+W^-b\bar{b}$ cross section from diagrams h_1-h_{10} can be interpreted as the bW^- pair originating from a nearly on-shell anti-top decay, while the bW^+ pair is produced non-resonantly, either from a highly virtual top (diagrams h_1-h_4), or without an intermediate top as in the truly single-resonant diagrams h_5-h_{10} . The contributions from $t\bar{b}W^-$ cuts, which are not displayed in Figure 1, yield identical results, by virtue of CP -invariance. The calculation of the amplitudes in Figure 1 amounts to the calculation of the squared and phase-space integrated matrix element of the on-shell processes $e^+e^- \rightarrow tW^-\bar{b}$ and $e^+e^- \rightarrow \bar{t}W^+b$ in ordinary perturbation theory with no width added to top propagators and divergences regularized dimensionally for consistency with the calculation of the resonant contribution to (2). The result is parametrically of order α_{EW}^3 , and hence represents an NLO correction relative to the $\mathcal{O}(\alpha_{EW}^2 v)$ leading-order cross section.

Beyond the NLO non-resonant terms that we calculate in this paper, the NNLO contributions are given by the 3-loop cut diagrams containing the α_s -corrections to the amplitudes of Figure 1, while the next order in the δ -expansion of the two-loop diagrams contributes only at N³LO. It is also interesting to note that pure background diagrams, *i.e.* diagrams without any top lines, start to contribute to the imaginary parts of the short-distance coefficients $C_{4e}^{(k)}$ at N³LO through the $W^+W^-b\bar{b}$ cuts of pure EW 3-loop diagrams. An exception to this are the three-particle final states with resonant decay of one of the particles to $W^+W^-b\bar{b}$ with large branching fraction as discussed in the previous section.

Turning now to the calculation, it proves convenient to cast the contributions from diagrams h_1-h_{10} (at order δ^0 and for $m_b = 0$) in the form

$$\int_{\Delta^2}^{m_t^2} dp_t^2 (m_t^2 - p_t^2)^{\frac{d-3}{2}} H_i\left(\frac{p_t^2}{m_t^2}, \frac{M_W^2}{m_t^2}\right) \quad (10)$$

where we have introduced the variable

$$p_t^2 = (p_b + p_{W^+})^2, \quad (11)$$

¹Recall that applying the Cutkosky rule for an internal line leads to the replacement of the propagator by its imaginary part. The leading term obtained by the expansion of the imaginary part in the hard region leads to a Dirac delta function, which is interpreted as if a top line with no self-energy insertion is cut.

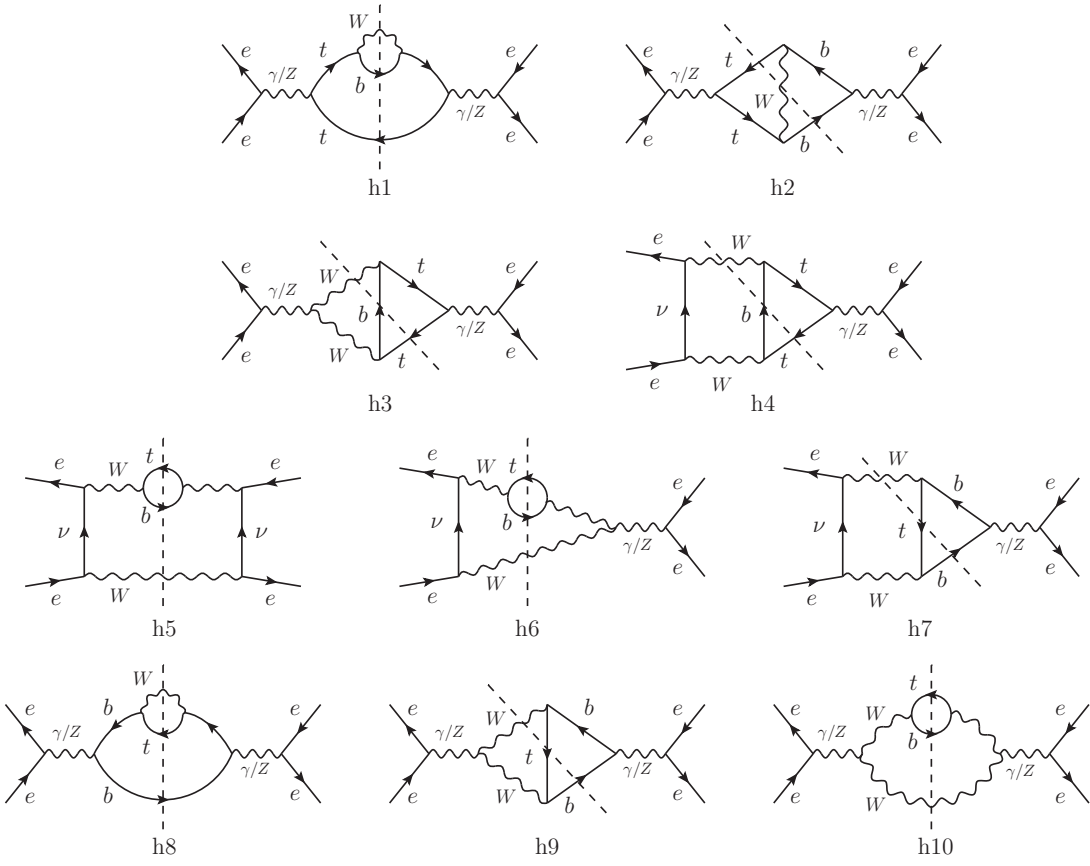


Figure 1: Two-loop forward-scattering amplitude diagrams with $\bar{t}bW^+$ cuts. $t\bar{b}W^-$ cuts and symmetric diagrams are not shown.

which corresponds to the invariant mass of the bW^+ system formed by the b and W^+ lines that are cut. For diagrams h_1 – h_4 , where the bW^+ system comes from the decay of the top line, the momentum p_t corresponds to the momentum of the top line. The upper limit on the p_t^2 integration in (10) corresponds to the kinematic limit associated to the $\bar{t}bW^+$ final state when $\delta \rightarrow 0$. The kinematic lower limit is given by $\Delta^2 = M_W^2$. The case of loose cuts on the bW^+ and $\bar{b}W^-$ invariant masses that are discussed in Section 4 can be incorporated easily in the computation of the four-electron matching coefficients by setting the lower bound of the p_t^2 integration to $\Delta^2 = m_t^2 - \Lambda^2$, with the parameter $\Lambda \equiv \Lambda_-$ defined in (19) below. The factor $(m_t^2 - p_t^2)^{(d-3)/2}$ in (10) regularizes the endpoint singularity in diagram h_1 at $p_t^2 = m_t^2$ due to the two top propagators that make H_1 behave as

$$H_1\left(\frac{p_t^2}{m_t^2}, \frac{M_W^2}{m_t^2}\right) \xrightarrow{p_t^2 \rightarrow m_t^2} \text{const} \times \frac{1}{(m_t^2 - p_t^2)^2}. \quad (12)$$

The use of dimensional regularization within the threshold expansion thus provides a

natural way to regularize the phase-space singularities in the hard region where the top propagators have no width. Dimensional regularization *must* be used for consistency, when the pure QCD calculation is performed with the dimensionally regularized non-relativistic effective theory. In the calculation of the other diagrams h_2 – h_{10} we can set $d = 4$, since they contain at most one internal top propagator leading to an integrable square-root endpoint singularity in (10).

The result of the calculation can be written as

$$\begin{aligned}
\sigma_{\text{non-res}}^{(1)} = & \frac{32\pi^2\alpha^2}{s} \frac{\Gamma_t^{\text{Born}}}{m_t} \left\{ \left[Q_t^2 C_{\gamma\gamma}(s) - 2v_t Q_t C_{\gamma Z}(s) + C_{ZZ}(s) v_t^2 \right] \frac{6\sqrt{2}}{\pi^2} \frac{m_t}{\Lambda} \right. \\
& + C_{\gamma\gamma}(s) \left[Q_t^2 h_1^V + 2Q_b Q_t h_2^V + 2Q_t h_3^V + Q_b^2 h_8 + 2Q_b h_9 + h_{10} \right] \\
& + C_{\gamma Z}(s) \left[-2Q_t v_t h_1^V + 2Q_t a_t h_1^{VA} - 2(Q_b v_t + Q_t(v_b + a_b)) h_2^V \right. \\
& \quad \left. - 2a_t Q_b h_2^A - 2v_t h_3^V + 2a_t h_3^A - 2\frac{c_w}{s_w} Q_t h_3^V \right. \\
& \quad \left. - 2Q_b(v_b + a_b) h_8 - 2\left(v_b + a_b + Q_b \frac{c_w}{s_w}\right) h_9 - 2\frac{c_w}{s_w} h_{10} \right] \\
& + C_{ZZ}(s) \left[v_t^2 h_1^V + a_t^2 h_1^A - 2v_t a_t h_1^{VA} + 2(v_b + a_b)(v_t h_2^V + a_t h_2^A) \right. \\
& \quad \left. + 2\frac{c_w}{s_w}(v_t h_3^V - a_t h_3^A) + (v_b + a_b)^2 h_8 + 2\frac{c_w}{s_w}(v_b + a_b) h_9 + \frac{c_w^2}{s_w^2} h_{10} \right] \\
& + C_\gamma(s) \left[Q_t h_4^V + h_6 + Q_b h_7 \right] \\
& \left. + C_Z(s) \left[v_t h_4^V + a_t h_4^A + \frac{c_w}{s_w} h_6 + (v_b + a_b) h_7 \right] + \frac{1}{s_w^4} h_5 \right\}, \tag{13}
\end{aligned}$$

where the functions

$$\begin{aligned}
C_{\gamma\gamma}(s) = & -Q_e^2 \frac{m_t^2}{4s}, \quad C_{\gamma Z}(s) = \frac{Q_e v_e m_t^2}{4(s - M_Z^2)}, \quad C_{ZZ}(s) = -\frac{s(v_e^2 + a_e^2)m_t^2}{4(s - M_Z^2)^2}, \\
C_\gamma(s) = & \frac{Q_e m_t^2}{s_w^2 s}, \quad C_Z(s) = \frac{(v_e + a_e)m_t^2}{s_w^2(s - M_Z^2)} \tag{14}
\end{aligned}$$

retain the exact s -dependence from the photon and Z -boson propagators, and

$$\Gamma_t^{\text{Born}} = \frac{\alpha |V_{tb}|^2 m_t}{16s_w^2} \frac{(1-x)^2(1+2x)}{x} \tag{15}$$

with $x = M_W^2/m_t^2$ is the tree-level top decay width obtained from $t \rightarrow bW^+$ with the bottom-quark mass set to zero. The dimensionless functions

$$h_i^X \equiv h_i^X(x, \Delta^2/m_t^2) \tag{16}$$

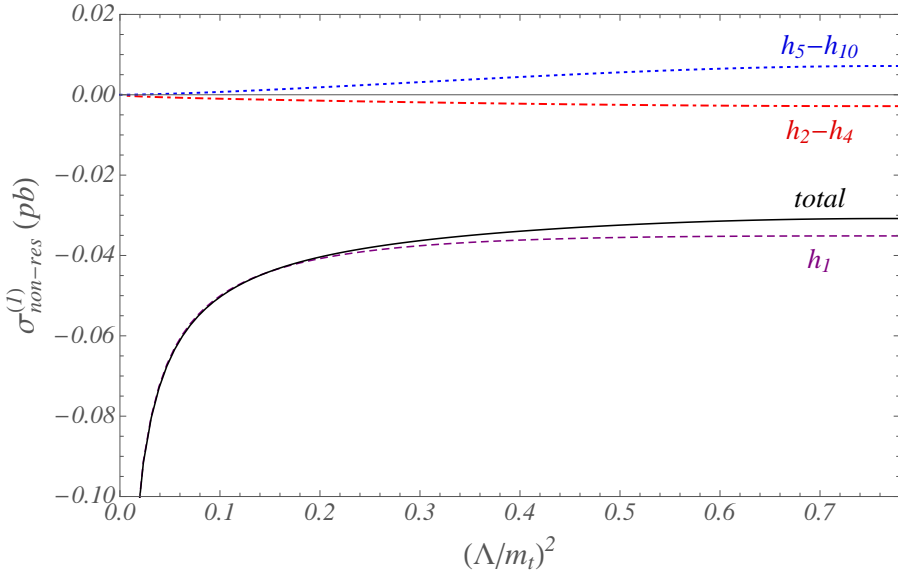


Figure 2: NLO non-resonant contributions to the cross sections computed at $s = 4m_t^2$ as a function of $(\Lambda/m_t)^2$, and with values for the input parameters given in (20). The maximal value of $(\Lambda/m_t)^2$ corresponding to the total cross section equals $1 - M_W^2/m_t^2 = 0.7815$. The solid (black) line is the total contribution $\sigma_{\text{non-res}}^{(1)}$ in (13), and the contributions from the diagram h_1 , from the sum of diagrams h_2-h_4 and from the truly single-resonant diagrams h_5-h_{10} are shown by the dashed (purple), dash-dotted (red) and dotted (blue) lines, respectively.

with $X = V, A, VA$, are obtained from diagrams $i = 1, \dots, 10$, and depend only on the ratios² $(M_W/m_t)^2$ and $(\Delta/m_t)^2$ but not on the centre-of-mass energy \sqrt{s} . To define the function h_1^V we subtracted from the integrand of diagram h_1 its leading singular behaviour as $p_t^2 \rightarrow m_t^2$ (see (33) in Appendix A). Adding back the subtracted expression yields the terms in the first line of (13) upon p_t^2 integration. Integral representations of the functions h_i^X which can easily be evaluated numerically are provided in the Appendix.

At NLO we could put $s = 4m_t^2$ in the $C_i(s)$ functions appearing in (14) and in the overall $1/s$ factor; keeping the exact energy dependence slightly improves the quality of the effective field theory (EFT) expansion. Since this energy dependence is mild compared to that of the resonant contributions within the range of energies relevant for the threshold region, the non-resonant contribution $\sigma_{\text{non-res}}^{(1)}$ results in an almost constant shift of the cross section.

The size of the NLO non-resonant contributions to the cross section evaluated at $s = 4m_t^2$ is shown in Figure 2 as a function of Λ^2/m_t^2 . In this Figure the total cross section corresponds to the maximal value of $\Lambda^2/m_t^2 = 1 - M_W^2/m_t^2 = 0.7815$. The

²Here we already allow for an invariant-mass cut on p_t^2 as discussed in Section 4. With no cut, $\Delta = M_W$ and $\Lambda = \sqrt{m_t^2 - M_W^2}$ in (13).

analysis reveals that the total (solid line in Figure 2) is negative³ and follows closely the contribution from diagram h_1 alone (dashed line) for all values of Λ^2 . The sum of the contributions of diagrams h_2-h_4 (dash-dotted line), where the bW^+ is produced from a highly virtual top quark, is rather small, less than 3 fb for all values of Λ^2 . The individual contributions from diagrams h_3 and h_4 are comparable in size with that of h_1 , but they cancel to a large extent. The sum of the truly single-resonant diagrams h_5-h_{10} (dotted line in Figure 2) is positive and also small, reaching at most 7 fb for the total cross section (*i.e.* when $\Lambda^2 = m_t^2 - M_W^2$). The smallness of the single-resonant contributions is due to large cancellations among diagrams h_5 , h_6 , and h_{10} which individually become more important than diagram h_1 for large values of Λ^2 .

For easy use we provide a compact fit formula for the NLO non-resonant contributions to the total cross section (corresponding to $\Lambda^2/m_t^2 = 1 - x$) in a reasonable range of top-mass values. In the range $m_t = 160\text{--}180$ GeV, a quadratic fit to the functions $h_i^X(x, x)$,

$$h_i^{X,\text{fit}}(x, x) = a + b \delta_{m_t} + c \delta_{m_t}^2 \quad , \quad \delta_{m_t} = \frac{m_t}{170 \text{ GeV}} - 1 \, , \quad (17)$$

is accurate to a precision better than one per mille. The coefficients a, b, c are given in Table 1. When the functions $h_i^{X,\text{fit}}(x, x)$ are combined into the total non-resonant contribution $\sigma_{\text{non-res}}^{(1)}$ according to (13), the precision of the quadratic fit compared to an exact (numerical) evaluation is better than $5 \cdot 10^{-5}$ for $160 \text{ GeV} \leq m_t \leq 180 \text{ GeV}$. Omitting the quadratic term in $h_i^{X,\text{fit}}(x, x)$, *i.e.* setting the c -coefficients to zero, the precision of $\sigma_{\text{non-res}}^{(1)}$ is still about one per mille or better.

4 Invariant-mass cuts in the effective theory

The measurement of the $t\bar{t}$ threshold shape under realistic experimental conditions will require to apply cuts in the kinematic variables of the observed particles in order to select $W^+W^-b\bar{b}$ events. For a general treatment of such phase-space cuts the EFT framework will have to be modified, and the bottom-quark and W -boson degrees of freedom and eventually those of their decay products have to be included. However, cuts on kinematic variables that are not sensitive to the angular or momentum distributions of the top decay products, such as cuts on the invariant masses of the bW^+ and $\bar{b}W^-$ subsystems, can be implemented in the unstable-particle effective-theory calculation, as discussed in [35,36,37].

We consider symmetric cuts on the invariant masses of the top (M_t) and anti-top ($M_{\bar{t}}$) decay products of the form

$$m_t - \Delta M_t \leq M_{t,\bar{t}} \leq m_t + \Delta M_t \, , \quad (18)$$

³The non-resonant cross section can be negative, since it is defined by analytic continuation to four dimensions of an expression that is divergent without regularization. Only the sum of resonant and non-resonant terms in (2) represents a physical quantity.

	a	b	c
h_1^V	1.292	-0.4022	1.024
h_1^A	-0.1631	-0.06325	0.1056
h_1^{VA}	-0.1286	-0.05451	0.08804
h_2^V	0.009852	-0.05238	-0.005537
h_2^A	0.001222	-0.001931	-0.005601
h_3^V	-0.4132	-0.8710	-0.2679
h_3^A	-0.04729	-0.1324	-0.05029
h_4^V	0.05962	0.08954	0.02671
h_4^A	-0.006691	-0.01716	-0.005359
h_5	0.005727	0.01925	0.02413
h_6	0.07369	0.2965	0.3855
h_7	0.001891	0.006638	0.004723
h_8	-0.007086	-0.01070	0.009648
h_9	-0.02321	-0.06746	-0.02936
h_{10}	-0.5453	-2.282	-3.081

Table 1: Coefficients for the fit functions $h_i^{X,\text{fit}}(x, x)$.

or equivalently

$$-\Lambda_-^2 \leq M_{t,\bar{t}}^2 - m_t^2 \leq \Lambda_+^2, \quad (19)$$

with $\Lambda_{\mp}^2 = 2m_t\Delta M_t \mp \Delta M_t^2$. Invariant-mass cuts on the top decay products translate to cuts on the momenta of the top (p_t) and anti-top ($p_{\bar{t}}$) circulating in the potential and hard loops of the e^+e^- forward-scattering amplitude. The cuts of the form (19) can be implemented by inserting a product of step-functions $\theta(\Lambda_+^2 - [p_t^2 - m_t^2])\theta(p_t^2 - m_t^2 + \Lambda_-^2)$, and similarly for $p_{\bar{t}}^2$, in the cut loop integral. In the effective theory the same step functions have to be introduced into the loops in the matrix elements of the resonant contributions, which reproduce the potential region of the full-theory diagrams. In the hard region, these step functions modify the calculation of the matching coefficients of the four-electron operators, which then become dependent on the invariant-mass cuts Λ_{\mp}^2 . At NLO this dependence enters explicitly through the lower limit in the integration that defines the h_i^X functions, see (10), (16). At this order, no dependence on the upper invariant-mass cut Λ_+^2 appears because the phase-space integration of the $\bar{t}bW^+$ final state in the hard diagrams of Figure 1 sets an upper kinematic limit $p_t^2 \leq m_t^2$; hence we define $\Lambda \equiv \Lambda_-$.

The two limiting cases for the invariant-mass cut corresponding to a loose cut, $\Lambda_{\mp}^2 \sim m_t^2$ (corresponding to $\Delta M_t \sim m_t$), and a tight cut, $\Lambda_{\mp}^2 \sim m_t\Gamma_t$ (corresponding to $\Delta M_t \sim \Gamma_t$), yield particularly simple prescriptions for implementing invariant-mass cuts

in unstable-particle effective theory, as it has been discussed in the context of W -pair production near threshold [35]. For tight cuts the matching coefficients of the four-electron operators vanish because in the hard region we have $|p_t^2 - m_t^2| \gg \Lambda_{\mp}^2$. Then the expansion of the product of step functions in small variables provides the factor $\theta(-|p_t^2 - m_t^2|) = 0$. Therefore four-electron operators do not contribute to the cross section for tight invariant-mass cuts. The same does not apply for the contributions from the resonant part, because there $p_t^2 - m_t^2 = 2m_t r_0 - \vec{r}^2 \sim \Lambda_{\mp}^2$, since the residual momentum $r = (r_0, \vec{r})$ has the characteristic scaling of the potential region $r \sim (m_t v^2, m_t v)$. The situation is reversed if we consider loose cuts. In this case the implementation of invariant-mass cuts on the loop integrals from the effective theory has no effect at the leading order because we can drop the momentum dependence from the step function following the assumption $\Lambda_{\mp}^2 \gg m_t r_0, \vec{r}^2 \sim (m_t v)^2$, and we are left with $\theta(\Lambda_-^2)\theta(\Lambda_+^2) = 1$. In particular, this means that the NLO QCD interference contributions are not affected by loose cuts and thus vanish, as it happens for the total cross section. The latter is confirmed by the calculation of the QCD interference effect with an invariant mass cut satisfying $\Lambda_{\mp}^2 \gg m_t \Gamma_t$ [37], which yields a correction of order $m_t \Gamma_t^2 / \Lambda_{\mp}^3$ relative to the LO resonant term, which is indeed parametrically suppressed relative to a NLO correction of order $\sqrt{\alpha_{EW}}$ when $\Lambda_{\mp} \sim m_t$. However, as already mentioned, the loose cut needs to be taken into account in the calculation of the matching coefficients of the four-electron operators as done in Section 3.

It is interesting to compare the above procedure for the treatment of invariant-mass cuts in the unstable-particle effective theory with the *phase-space matching* approach introduced in the recent paper [37]. In the latter, the matching coefficients of the four-electron operators (called *phase-space matching* conditions) are determined in the following way. First, cuts of the form (18) are introduced on the top and anti-top momenta in the NRQCD loop diagrams, the latter corresponding to the resonant contributions in (2). Then the resulting cut loop integrals are expanded assuming that $\Lambda^2 \gg (m_t v)^2, m_t \Gamma_t$, which is formally correct as long as $\Lambda^2 \ll m_t^2$, since NRQCD describes the non-relativistic $t\bar{t}$ configurations and Λ^2 acts effectively as a cut on the non-relativistic momentum \vec{r}^2 . The Λ -dependent terms that result from this expansion yield a series of the form $\Gamma_t / \Lambda \times \sum_{n,m} [(m_t \Gamma_t / \Lambda^2)^n \times (\Lambda^2 / m_t^2)^m]$, with $n, m = 0, 1, \dots$. Powers of Λ^2 / m_t^2 enter first from cut diagrams with NNLO relativistic corrections that come with a factor \vec{r}^2 / m_t^2 , and are a signal of the breakdown of the series for $\Lambda \sim m_t$. The whole computation is equivalent to the non-relativistic expansion of the full-theory squared matrix elements containing the double-resonant diagrams for $e^+e^- \rightarrow t\bar{t} \rightarrow W^+W^-b\bar{b}$ and their interference with the diagrams for $e^+e^- \rightarrow W^+W^-b\bar{b}$ having only either the top or the anti-top in intermediate stages. Contrary to the method presented in the present paper, the non-resonant contributions to the full-theory matrix element coming from the square of single-top and pure background diagrams (the so-called remainder contributions in [37]) cannot be determined within the phase-space matching approach. The path taken by the authors of [37] is to compute the remainder contributions by comparing the NRQCD cross section with the relativistic Born cross section for $e^+e^- \rightarrow W^+W^-b\bar{b}$ as obtained with MadGraph/MadEvent [41]. The comparison yielded that the remainder terms are

below 5 fb for invariant-mass cuts $\Delta M_t \leq 35$ GeV, and hence were neglected given the theoretical precision goal aimed at in [37]. This approach is currently not feasible at NNLO, where no external tools exist to determine the remainder terms, and the α_s -correction to the coefficient functions of the four-electron operators must be determined by the methods described in the present paper. Also, the present method allows us to consider very loose cuts with $\Lambda \sim m_t$ up to the total cross section. On the other hand, assuming that there is no kinematic or dynamical enhancement in the QCD corrections to the remainder contributions, part of the α_s -corrections to the non-resonant contributions has already been analyzed in [37], again for intermediate-sized cuts, which in our approach correspond to NNLO contributions not yet known.

We have checked that the expansion of our result (13) for the non-resonant contributions in $\Lambda^2/m_t^2 \ll 1$ matches the series obtained in [37] when $\alpha_s = 0$ for the Γ_t/Λ and $\Gamma_t\Lambda/m_t^2$ terms. In this limit, diagrams h_5-h_{10} , which are part of the remainder contributions not calculable within the phase-space matching approach, first contribute with $\Gamma_t\Lambda^3/m_t^4$ terms.

4.1 Comparison to the $e^+e^- \rightarrow W^+W^-b\bar{b}$ Born cross section from MadGraph

Before discussing the final result for the $W^+W^-b\bar{b}$ cross section in the top anti-top resonance region including Coulomb resummation, we compare the EFT prediction without strong-interaction effects to the full-theory (Standard Model) $W^+W^-b\bar{b}$ Born cross section computed with MadGraph/MadEvent [41]. The input parameters are chosen to be

$$\begin{aligned} M_Z &= 91.1876 \text{ GeV} , & M_W &= 80.398 \text{ GeV} , & M_H &= 120 \text{ GeV} , \\ G_\mu &= 1.166367 \times 10^{-5} \text{ GeV}^{-2} , & m_t &= 172.0 \text{ GeV} , & V_{tb} &= 1 , \end{aligned} \quad (20)$$

whereas the on-shell Weinberg angle $c_w = M_W/M_Z$ and the fine-structure constant in the G_μ -scheme, $\alpha \equiv \sqrt{2}G_\mu M_W^2 s_w^2/\pi$, are derived quantities. Tree-level amplitudes generated by MadGraph implement the fixed-width prescription for the top-quark propagator. For the numerical value of Γ_t we use the Born formula (15) in both MadGraph and the EFT predictions, thus neglecting α_s -corrections to the top-width value. MadGraph uses a finite bottom-quark mass whereas we neglect it in the EFT calculation.

In Figure 3 we analyze the invariant-mass cut dependence of the $e^+e^- \rightarrow W^+W^-b\bar{b}$ Born cross section calculated at $s = 4m_t^2$. The values shown there range from the ΔM_t value corresponding to $\Lambda^2 = m_t\Gamma_t$ up to the maximum value allowed by the kinematics, $\Delta M_{t,\max} = m_t - M_W$. The (red) triangle-shaped dots represent the Standard-Model $e^+e^- \rightarrow W^+W^-b\bar{b}$ Born cross section computed with MadGraph, while for the (blue) circular dots we have omitted in the MadGraph amplitude generation the diagrams with internal Higgs lines. The shaded bands represent the statistical uncertainties on the MadEvent integration, calculated as the cross section divided by the square root of the number of selected events that pass the invariant-mass cut. The small difference between both sets of points for large values of ΔM_t is explained below. The lower solid (blue)

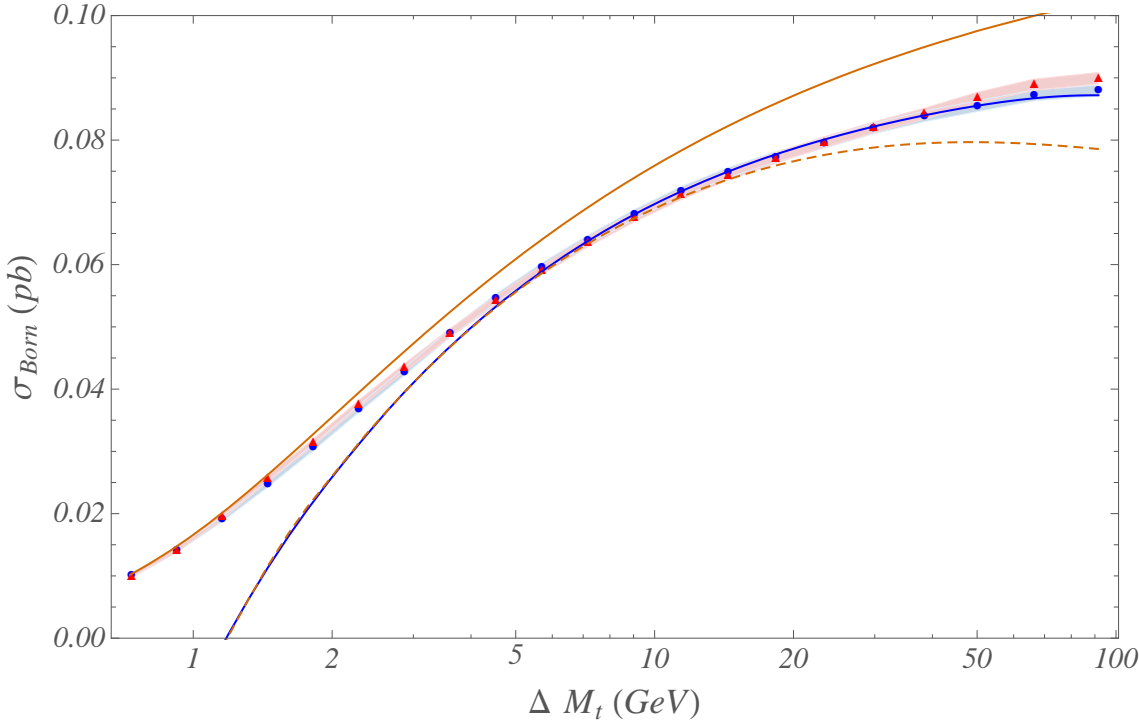


Figure 3: Invariant-mass cut dependence of the $e^+e^- \rightarrow W^+W^-b\bar{b}$ Born cross section at $s = 4m_t^2$. The ΔM_t values range from $\Delta M_t = 0.734$ GeV corresponding to $\Lambda^2 = m_t \Gamma_t$ to the kinematic bound, $\Delta M_{t,\max} = m_t - M_W = 91.602$ GeV. The (red) triangle-shaped dots represent the Standard-Model cross section computed with MadGraph; for the (blue) circular dots we have omitted the diagrams with internal Higgs lines. The corresponding shaded bands show the statistical uncertainty of the MadEvent integration. Lower solid (blue) line: NNLO EFT approximation given in (21). Upper solid (brown) line: LO EFT tight-cut prediction (30). Dashed (brown) line: $\alpha_s = 0$ NNLO results with invariant-mass cuts from [37] (not including the remainder contributions). The LO Born EFT result, which does not depend on ΔM_t , is not shown in the Figure. It equals $\sigma_{t\bar{t}, \alpha_s=0}^{(0)} = 0.1139$ pb at $s = 4m_t^2$.

line is the NNLO EFT approximation to the full Born result, given by

$$\sigma_{\text{Born}} = \sigma_{t\bar{t}, \alpha_s=0}^{(0)} + \sigma_{\text{non-res}}^{(1)} + \sigma_{v^2}^{(2)} + \sigma_{P\text{-wave}}^{(2)} + \sigma_{\text{bil}}^{(2)} + \sigma_{\text{abs}}^{(2)}. \quad (21)$$

The first term on the right-hand side is the LO cross section (6), with the QCD radiative corrections switched off (*i.e.* setting $\alpha_s = 0$). At $s = 4m_t^2$ it amounts to $\sigma_{t\bar{t}, \alpha_s=0}^{(0)} = 0.1139$ pb. Loose cuts on the bW^+ and $\bar{b}W^-$ invariant masses contribute first at the NLO in the EFT power counting through the non-resonant contributions $\sigma_{\text{non-res}}^{(1)}$ discussed in Section 3. The v^2 -suppressed S -wave current describing the top anti-top pair production in the effective theory gives the NNLO correction $\sigma_{v^2}^{(2)}$. Using the non-relativistic equation

of motion for the top quark it can be taken into account by replacing $G_C^{(0)}(0, 0; \mathcal{E}) \rightarrow (1 - \mathcal{E}/(3m_t)) G_C^{(0)}(0, 0; \mathcal{E})$ in (6). The term $\sigma_{P\text{-wave}}^{(2)}$ is generated by the matrix element of the production (decay) P -wave operators, which are v -suppressed with respect the leading S -wave operators (3). It reads

$$\sigma_{P\text{-wave}}^{(2)} = \left[(C_{p, P\text{-wave}}^{(v)})^2 + (C_{p, P\text{-wave}}^{(a)})^2 \right] \frac{4N_c}{3m_t^2} \text{Im } G_{P\text{-wave}}^{(2)}, \quad (22)$$

with

$$\begin{aligned} C_{p, P\text{-wave}}^{(v)} &= 4\pi\alpha \frac{v_e a_t}{s - M_Z^2}, \\ C_{p, P\text{-wave}}^{(a)} &= -4\pi\alpha \frac{a_e a_t}{s - M_Z^2}, \end{aligned} \quad (23)$$

and

$$G_{P\text{-wave}}^{(2)} = \frac{m_t^4}{4\pi} \left(-\frac{\mathcal{E}}{m_t} \right)^{3/2}, \quad (24)$$

the P -wave component of the free Green function at zero distance that can be obtained by setting $\alpha_s = 0$ in the $\overline{\text{MS}}$ -renormalized expression for the P -wave Coulomb Green function [14]. The term $\sigma_{\text{bil}}^{(2)}$ originates from the effective-theory matrix elements with a single insertion of the NNLO corrections to the bilinear quark terms in the non-relativistic Lagrangian, $\delta\mathcal{L} = 1/(8m_t^3) \times \psi_t^\dagger (\vec{\partial}^2 + im_t\Gamma_t)^2 \psi_t$, and the corresponding anti-quark terms. Written as corrections to the zero-distance Green function, it reads

$$\sigma_{\text{bil}}^{(2)} = \left[C_p^{(v)2} + C_p^{(a)2} \right] 2N_c \text{Im} \left(\delta G_{\text{kin}}^{(2)} + \delta G_{\Gamma_t}^{(2)} + \delta G_{\Gamma_t^2}^{(2)} \right), \quad (25)$$

where $\delta G_{\text{kin}}^{(2)}$, $\delta G_{\Gamma_t}^{(2)}$ and $\delta G_{\Gamma_t^2}^{(2)}$ correspond to the insertion of the $\vec{\partial}^4/(8m_t^3)$, $i\Gamma_t\vec{\partial}^2/(4m_t^2)$ and $-\Gamma_t^2/(8m_t)$ operators, respectively, and read

$$\delta G_{\text{kin}}^{(2)} = \frac{5m_t^2}{32\pi} \left(-\frac{\mathcal{E}}{m_t} \right)^{3/2}, \quad (26)$$

$$\delta G_{\Gamma_t}^{(2)} = \frac{3m_t^2}{16\pi} i \frac{\Gamma_t}{m_t} \left(-\frac{\mathcal{E}}{m_t} \right)^{1/2}, \quad (27)$$

$$\delta G_{\Gamma_t^2}^{(2)} = -\frac{1}{32\pi} \frac{\Gamma_t^2}{(-\mathcal{E}/m_t)^{1/2}}. \quad (28)$$

The terms $\delta G_{\Gamma_t}^{(2)}$ and $\delta G_{\Gamma_t^2}^{(2)}$ are pure electroweak contributions. While the former corresponds to the lifetime-dilatation correction studied in [31], $\delta G_{\Gamma_t^2}$ has not been considered so far among the NNLO electroweak corrections. Numerically, the latter term is rather small. Note that $\delta G_{\Gamma_t}^{(2)}$ can be obtained by replacing $m_t \rightarrow m_t - i\Gamma_t/2$ in (6) and expanding to first order in the correction; similarly, $\delta G_{\Gamma_t^2}^{(2)}$ follows from replacing

$\Gamma_t \rightarrow \Gamma_t + i\Gamma_t^2/(4m_t)$ in (6) and the first-order expansion in the correction. In both cases, only the term with $\alpha_s = 0$ is needed for comparison with the Born cross section. The last term in (21), $\sigma_{\text{abs}}^{(2)}$, arises from the absorptive parts in the matching coefficients of the production operators $\mathcal{O}_p^{(v)}$ and $\mathcal{O}_p^{(a)}$ that were determined in [31]. It reads

$$\sigma_{\text{abs}}^{(2)} = 2 [C_p^{(v)} C_p^{(v),\text{abs}} + C_p^{(a)} C_p^{(a),\text{abs}}] 2N_c \text{Re } G_0^{(0)}, \quad (29)$$

with $G_0^{(0)}$ the free Green function. The explicit expressions for the coefficients $C_p^{(v),\text{abs}}$ and $C_p^{(a),\text{abs}}$ can be found in [31] (there denoted $C_V^{bW,\text{abs}}$ and $C_A^{bW,\text{abs}}$, respectively).⁴ The term $\sigma_{\text{abs}}^{(2)}$ reproduces the interference of single-resonant and double-resonant $e^+e^- \rightarrow W^+W^-b\bar{b}$ diagrams in the kinematic region where both bW^+ and $\bar{b}W^-$ have invariant masses of order m_t . Within the threshold expansion [42], these contributions arise from precisely the cut diagrams h_1-h_4 in Figure 1, but with one hard and one potential loop, the latter corresponding to the loop containing the top and anti-top propagators. Let us recall that for the non-resonant contributions the two loop momenta have to be taken as hard, so the absorptive parts in $C_p^{(v),\text{abs}}$ and $C_p^{(a),\text{abs}}$ and the non-resonant contributions come from different loop-momentum regions and there is no double-counting. The additional v -suppression of the hard-potential with respect to the hard-hard contributions from diagrams h_1-h_4 is explained by the different power counting of the loop momentum in the hard ($r_0 \sim \vec{r} \sim m_t$) and potential ($r_0 \sim \vec{r}^2/m_t \sim m_t v^2$) regions. The sum of all the NNLO corrections in (21) gives a positive shift of 4.1 fb for $s = 4m_t^2$.

Already for values of the invariant-mass cut $\Delta M_t \gtrsim 5 \text{ GeV} \approx 3.5 \Gamma_t$ we find an excellent agreement between the full-theory Born cross section computed with MadGraph and the effective-theory prediction for loose cuts. To account for invariant-mass cuts in the range $\Delta M_t \lesssim \Gamma_t$ we need to implement the tight-cut prescription in the effective-theory calculation. This is done in the upper solid curve of Figure 3, which is obtained by introducing the proper step functions into the one-loop cut integral of the LO effective-theory result. Precisely, the LO tight-cut prediction reads

$$\sigma_{tt,\text{tight}}^{(0)} = [C_p^{(v)2} + C_p^{(a)2}] 2N_c \text{Im } G_{0,\text{tight}}^{(0)}, \quad (30)$$

with

$$\begin{aligned} \text{Im } G_{0,\text{tight}}^{(0)} &= \frac{\Gamma_t^2}{2} \int \frac{d^4 r}{(2\pi)^4} \frac{\theta(\Delta M_t + \frac{E}{2} + r_0 - \frac{\vec{r}^2}{2m_t}) \theta(\Delta M_t + \frac{E}{2} - r_0 - \frac{\vec{r}^2}{2m_t})}{\left[(\frac{E}{2} + r_0 - \frac{\vec{r}^2}{2m_t})^2 + \frac{\Gamma_t^2}{4} \right] \left[(\frac{E}{2} - r_0 - \frac{\vec{r}^2}{2m_t})^2 + \frac{\Gamma_t^2}{4} \right]} \\ &= \frac{m_t \Gamma_t}{4\pi^3} \int_0^{\frac{2\Delta M_t}{m_t}} \frac{dy}{y} \left(y + \frac{E}{m_t} \right)^{1/2} \left(\frac{1}{y - i\frac{\Gamma_t}{m_t}} \arctan \left(\frac{\frac{2\Delta M_t}{m_t} - y}{\frac{\Gamma_t}{m_t} + iy} \right) + \text{h.c.} \right), \end{aligned} \quad (31)$$

which we evaluate at $E = 0$ for the result displayed in Figure 3. We see that this expression agrees well with the full Born cross section for very small ΔM_t . The agreement

⁴The imaginary part of the field-rescaling factor called ϖ in [33,34] is taken into account in the calculation of these coefficients.

could be extended to larger values by implementing the cuts in the NNLO terms, but we do not pursue this here.

Finally, the dashed curve corresponds to the $\alpha_s = 0$ NNLO formula with invariant-mass cuts obtained in [37] (not including the remainder contributions), which contains the same NNLO pieces as our result (21) but for $\delta G_{\Gamma_t^2}$. As mentioned before, the pieces depending on the invariant-mass cut in the formula in [37] match the leading and sub-leading terms of the expansion in Λ^2/m_t^2 of our NLO non-resonant contributions, and the two results should therefore agree well when $\Delta M_t \ll \Delta M_{t,\max}$. Figure 3 demonstrates this and also shows that as expected, the difference between our result (solid blue line) and the formula from [37] increases with ΔM_t : at $\Delta M_t = 35$ GeV it amounts to about 4 fb, while for the total cross section ($\Delta M_{t,\max}$) it reaches almost 9 fb, which roughly agrees with the size of the single-top non-resonant contributions, that are not accounted for in the phase-space matching approach.

As mentioned above, Figure 3 shows two sets of MadGraph points. The red triangles represent the complete tree-level cross section. They agree with our effective-theory prediction for loose cuts $\Delta M_t \gtrsim 5$ GeV, but for $\Delta M_t \gtrsim 40$ GeV and for the total cross section they rise to values of up to 3 fb above our result. This small, but visible difference is mostly due to diagrams with intermediate Higgs lines which account for 2 fb of this difference. Eliminating the Higgs diagrams from the MadGraph amplitude gives the blue dots which agree with the effective-theory result also for large ΔM_t within the statistical uncertainty of the MadEvent integration. The Higgs contribution originates almost exclusively from phase-space regions where the $b\bar{b}$ invariant mass is close to the Higgs-mass value $M_H = 120$ GeV, *i.e.* from on-shell Higgs bosons decaying into a $b\bar{b}$ pair. Despite the smallness of the bottom Yukawa coupling, such diagrams can yield sizable contributions because the Higgs width is small and the branching fraction of $H \rightarrow b\bar{b}$ is large (about 70%). The distribution of the Higgs contributions with respect to the invariant masses of the bW^+ or $\bar{b}W^-$ pairs is relatively broad, while the same invariant-mass distributions of the contributions with (anti)top lines are sharply peaked around the top mass. This explains why the Higgs contributions are only visible for very loose or no cuts. Such small contributions from Higgs diagrams constitute a reducible background which can easily be eliminated by cuts on the $b\bar{b}$ invariant mass when one is only interested in the $t\bar{t}$ resonance region. This justifies that we have not considered contributions from nearly on-shell Higgs bosons in our effective-theory approach although they formally count as NLO contributions as explained in Section 2.2.

The energy dependence of the effective-theory prediction (21) for the total cross section (upper panel), $\Delta M_t = 15$ GeV (middle panel) and $\Delta M_t = 5$ GeV (lower panel) is shown in Figure 4 in the interval $\sqrt{s} = (334, 354)$ GeV. The blue dots correspond to the full-theory Born $W^+W^-b\bar{b}$ cross section, while the solid (blue) line is the corresponding prediction at NNLO from the unstable-particle effective-theory. For the total cross section the tiny difference between both results is mainly due to the Higgs contributions explained above. The agreement improves for smaller values of ΔM_t , as seen in the middle panel of Figure 4. For $\Delta M_t = 5$ GeV the effective-theory expansion quickly degrades as we move away from the threshold. This is evident below threshold, where

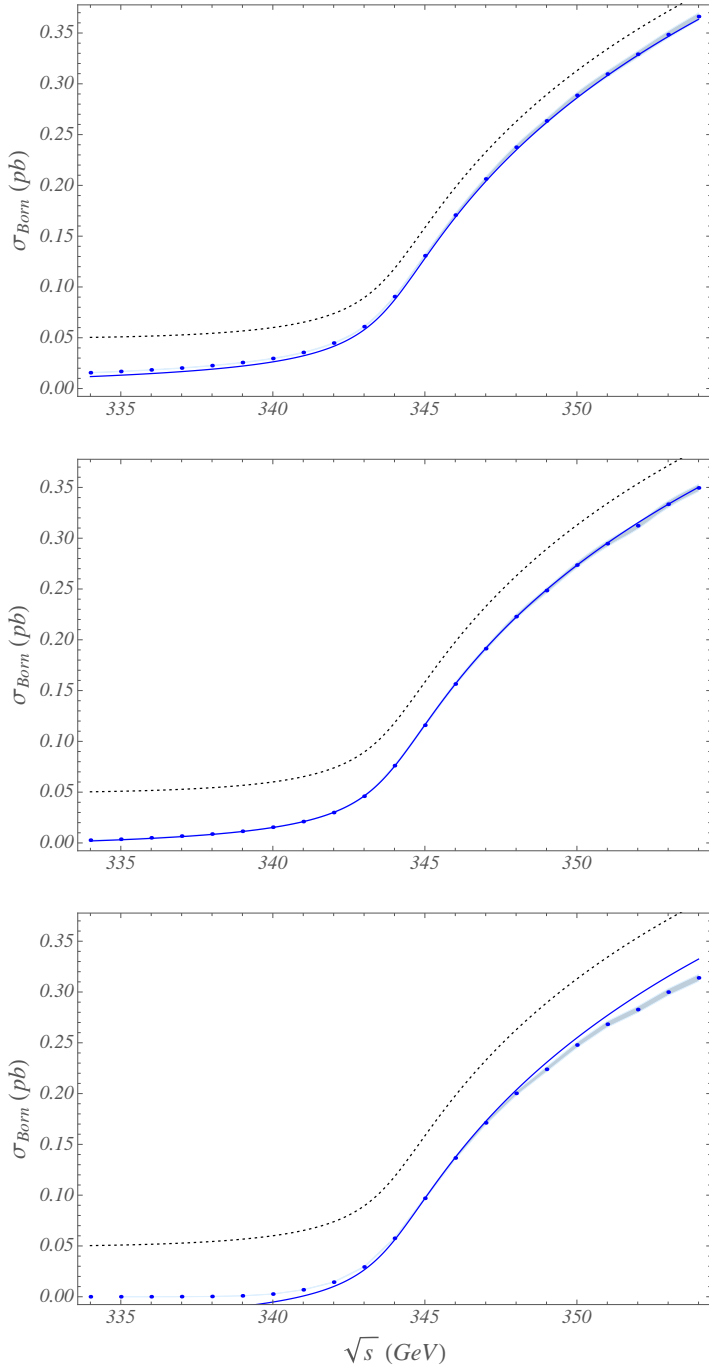


Figure 4: NNLO EFT approximation to the Born $W^+W^-b\bar{b}$ cross section with (solid blue line) and without (dotted black line) the NLO non-resonant contributions as a function of the centre-of-mass energy. Upper, middle and lower panels correspond to $\Delta M_t = (\Delta M_{t,\text{max}}, 15, 5)$ GeV. The (blue) dots are the full-theory result computed with MadGraph, and the shaded band is the statistical uncertainty of the MadEvent integration.

the effective-theory result becomes negative. The large negative shift of about 24–39 fb for the total cross section given by the NLO non-resonant contributions is clearly seen in Figure 4 once we draw the NNLO effective-theory result without the non-resonant contributions (dotted line). The shift becomes larger as we tighten the invariant-mass cut, up to 38–48 fb for $\Delta M_t = 15$ GeV.

5 Final results

In this section we compare the size of the NLO non-resonant and QED corrections to the LO effective-theory approximation (6) for the $e^+e^- \rightarrow W^+W^-b\bar{b}$ cross section. This now includes the summation of Coulomb corrections proportional to $(\alpha_s/v)^n$ to all orders in the strong coupling, which produces the characteristic peak structure in the top anti-top resonance region. As mentioned in Section 2.2, we do not discuss the pure NLO QCD corrections, which have already been studied in the literature. Moreover it is known that the NLO QCD corrections are rather large (and negative) and cancelled to a large extent by the NNLO QCD corrections [6,7,8,9,10,11,12]. Hence the conclusions that can be drawn by comparing the electroweak corrections with the NLO QCD corrections may not be valid once higher-order QCD corrections are considered. For the results in this section we choose $\alpha_s(30\text{ GeV}) = 0.142$ for the value of the QCD coupling that enters in the LO Coulomb Green function. The relative sizes of the NLO electroweak corrections with respect to the LO result are displayed in Figure 5.

The upper (blue) solid line shows the ratio $\sigma_{\text{QED}}^{(1)}/\sigma_{t\bar{t}}^{(0)}$ (in percent), where the QED correction $\sigma_{\text{QED}}^{(1)}$ is obtained as

$$\sigma_{\text{QED}}^{(1)} = \left(\sigma_{t\bar{t}}^{(0)} \Big|_{\alpha_s C_F \rightarrow \alpha_s C_F + \alpha Q_t^2} \right) - \sigma_{t\bar{t}}^{(0)}. \quad (32)$$

The QED contribution represents a correction of about 2% above threshold and rises to a maximum of 7% just below the peak. The lower (red) solid line is obtained as the ratio $\sigma_{\text{non-res}}^{(1)}/\sigma_{t\bar{t}}^{(0)}$ (in percent) with ΔM_t set by the kinematic bound. The non-resonant contributions give a constant negative shift of about 3% above threshold. Below threshold the relative size of the non-resonant corrections is very large, since the LO result rapidly vanishes, reaching up to 19%. Hence below threshold they represent the leading electroweak correction to the total $t\bar{t}$ cross section. The sum of both NLO electroweak corrections compared to the LO cross section is shown in the middle solid (black) line. We observe a partial cancellation of the QED and non-resonant corrections in the peak region and at energies above. A sensitivity to the invariant-mass cut ΔM_t in the bW^+ and $\bar{b}W^-$ subsystem enters first at NLO through the non-resonant contributions. Restricting the available phase-space for the final-state particles by tightening the invariant-mass cuts ΔM_t makes the non-resonant contributions even more important. This is shown by the dashed lines in Figure 5, corresponding to $\Delta M_t = 15$ GeV, for the relative size of the non-resonant correction (lower dashed line) and of the sum of the two electroweak corrections (middle dashed line).

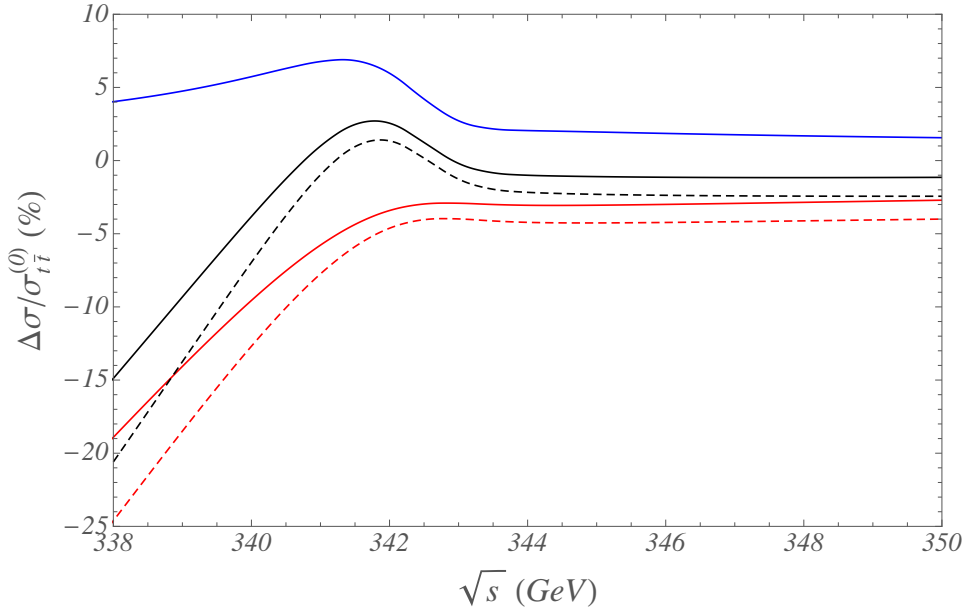


Figure 5: Relative sizes of the QED and non-resonant corrections with respect to the $t\bar{t}$ LO cross section in percent: $\sigma_{\text{QED}}^{(1)}/\sigma_{t\bar{t}}^{(0)}$ (upper solid blue line), $\sigma_{\text{non-res}}^{(1)}/\sigma_{t\bar{t}}^{(0)}$ for the total cross section (lower solid red line) and $\Delta M_t = 15$ GeV (lower dashed red line). The relative size of the sum of the QED and non-resonant corrections is represented by the middle (black) lines, for $\Delta M_{t,\text{max}}$ (solid) and $\Delta M_t = 15$ GeV (dashed).

Aside from the pure QCD corrections, the effective-theory NLO prediction for the $e^+e^- \rightarrow W^+W^-b\bar{b}$ cross section is displayed by the solid lines in Figure 6. The upper panel corresponds to the total cross section and for the lower panel $\Delta M_t = 15$ GeV. The absolute size of the non-resonant correction is given by the difference between the dashed lines, which only include the QED NLO correction, and the solid ones. These negative shifts amount to 27–35 fb for the total cross section and 39–46 fb for $\Delta M_t = 15$ GeV for \sqrt{s} in the interval (338, 350) GeV.

6 Summary

We presented an analysis of the $e^+e^- \rightarrow W^+W^-b\bar{b}$ process in the top anti-top resonance production region $\sqrt{s} \approx 2m_t$ extending the methods developed in [34,35] for W -pair production to the more complicated case of top quarks. Our result may be considered as the first complete NLO calculation of top-quark pair production near threshold, when the top width is accounted for, which necessarily requires to consider the final state $W^+W^-b\bar{b}$ for consistency. The result is valid for the total cross section and with invariant-mass cuts on the Wb systems as long as the cut ΔM_t is significantly larger than the top width. We also included the case of tight cuts in the comparison with the full-theory Born cross

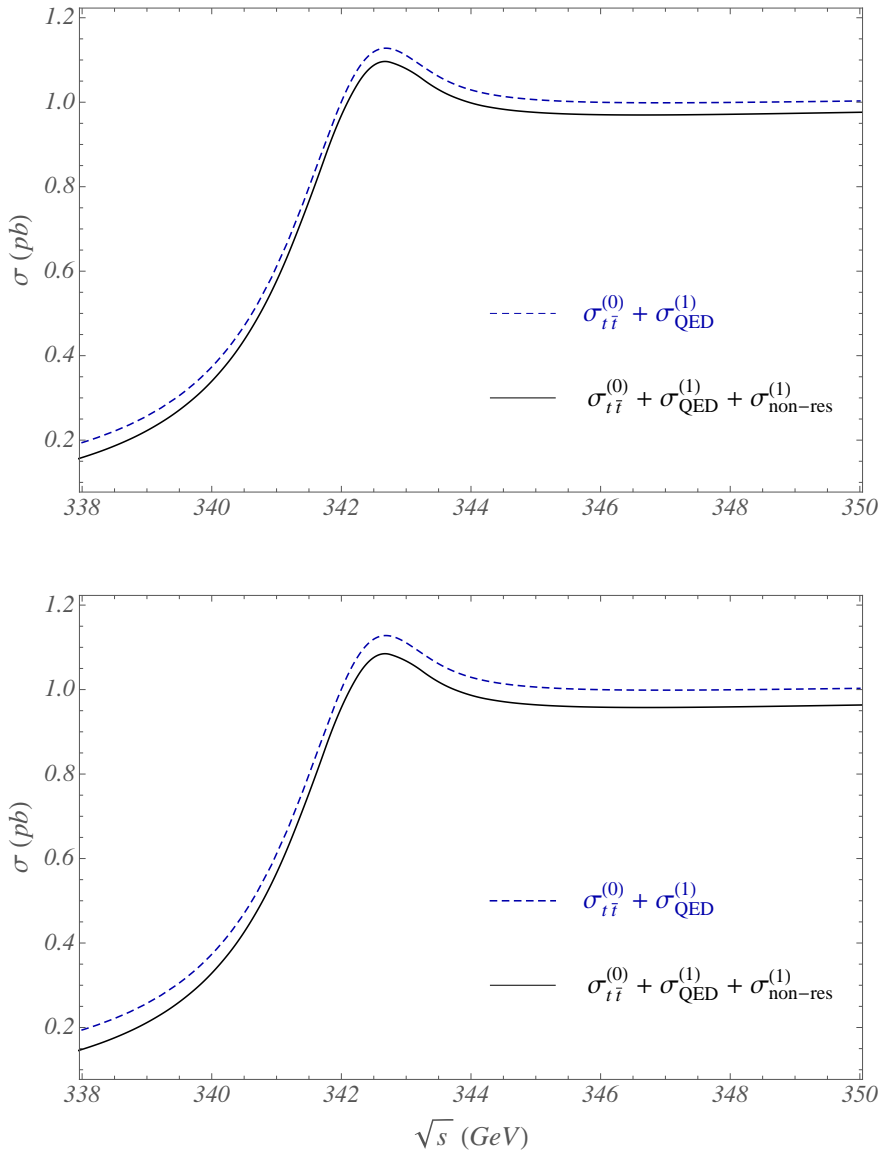


Figure 6: $e^+e^- \rightarrow W^+W^-b\bar{b}$ cross section with LO QCD effects and NLO electroweak corrections at energies close to threshold. The dashed (blue) lines represent $\sigma_{t\bar{t}}^{(0)} + \sigma_{\text{QED}}^{(1)}$ and the solid lines $\sigma_{t\bar{t}}^{(0)} + \sigma_{\text{QED}}^{(1)} + \sigma_{\text{non-res}}^{(1)}$. The results in the upper panel correspond to the total cross section ($\Delta M_t = \Delta M_{t,\text{max}}$), while for the lower panel $\Delta M_t = 15$ GeV.

section.

We find that the non-resonant contributions reduce the cross section in the top anti-top resonance peak region by up to 5%, which is relevant in view of the high-precision top mass and width determination anticipated at the ILC. In the energy region below the peak the non-resonant correction is significantly larger, since the resonant contribution rapidly decreases with energy, while the non-resonant one is nearly energy-independent.

These conclusions agree with the recent work [37]. The approach pursued in the present paper allows us to extend them to the case of the total cross section and rather loose cuts, and it also determines the full non-resonant background within the effective theory approach rather than using external information. The final numerical result turns out to be dominated by the off-shell contribution from the double-resonant diagram h_1 , but only due to a large cancellation within classes of other diagrams.

Our work provides a step towards predictions including consistently the top width in effective theory calculations of $t\bar{t}$ production, more precisely $W^+W^-b\bar{b}$ production, near threshold also in higher orders in the expansion in α_s , α_{EW} and $\delta \sim v^2$. Going to higher orders will eventually be required to cancel the finite-width divergences that appear in the NNLO and N³LO pure QCD calculations that are already complete or near completion.

Acknowledgment

We thank A.H. Hoang for comments on the manuscript. This work is supported by the DFG Sonderforschungsbereich/Transregio 9 “Computergestützte Theoretische Teilchenphysik”. Feynman diagrams have been drawn with the packages AXODRAW [43] and JAXODRAW [44]. We acknowledge the use of the computer programs FORM [45] and FEYNCALC [46] for some parts of the calculation.

A Formulae for the h_i^X functions

We present here integral representations of the functions $h_i^X(x, y)$ defined in (16) and used in (13). Their arguments are $x = M_W^2/m_t^2$ and the cut-dependent integration limit $y = \Delta^2/m_t^2 = 1 - \Lambda^2/m_t^2$ satisfying $x \leq y \leq 1$.

Diagram h_1 :

$$\begin{aligned} h_1^V(x, y) &= -\frac{1}{64\pi^2} \int_y^1 dt (1-t)^{-3/2} \left[\frac{\Gamma_t(t)}{\Gamma_t^{\text{Born}}} \sqrt{9-t} \left(27 + 73t - 3t^2 - t^3 \right) - 192\sqrt{2} \right], \\ h_1^A(x, y) &= -\frac{1}{64\pi^2} \int_y^1 dt \sqrt{\frac{9-t}{1-t}} \frac{\Gamma_t(t)}{\Gamma_t^{\text{Born}}} \left(27 + 4t + t^2 \right), \\ h_1^{VA}(x, y) &= -\frac{1}{64\pi^2} \int_y^1 dt \sqrt{\frac{9-t}{1-t}} \frac{\Gamma_t(t)}{\Gamma_t^{\text{Born}}} \left(27 - 2t - t^2 \right), \end{aligned} \quad (33)$$

with the “off-shell” top width defined as

$$\Gamma_t(t) = \Gamma_t^{\text{Born}} \frac{\left(1 - \frac{x}{t}\right)^2 \left(1 + \frac{2x}{t}\right) t}{(1-x)^2(1+2x)}. \quad (34)$$

The last term within the square brackets in the first line of (33) is a subtraction term which regularizes the integrand at $t = 1$. The integration of minus this subtraction

term using dimensional regularization yields the terms quoted in the first line on the right-hand side of (13).

Diagram h_2 :

$$h_2^V(x, y) = \frac{1}{4\pi^2(x-1)^2(2x+1)} \int_y^1 dt \left\{ \begin{aligned} & \frac{t(2x^2 + 7x - 5) - x(2x^2 + 15x + 31)}{1-t} f_+(t, x) \\ & + \frac{t-x}{16t^2} \sqrt{\frac{9-t}{1-t}} \left(t^4 + t^3(x+4) - t^2(2x^2 + 12x + 53) - tx(24x + 85) - 6x^2 \right) \end{aligned} \right\}, \quad (35)$$

$$h_2^A(x, y) = \frac{1}{4\pi^2(x-1)^2(2x+1)} \int_y^1 dt \left\{ \begin{aligned} & \frac{t(2x^2 + 5x - 3) - x(2x^2 + 13x + 17)}{1-t} f_+(t, x) \\ & + \frac{t-x}{16t^2} \sqrt{\frac{9-t}{1-t}} \left(t^4 + t^3(x+2) - t^2(2x^2 + 14x + 27) - tx(20x + 59) + 6x^2 \right) \end{aligned} \right\}, \quad (36)$$

with

$$f_{\pm}(t, x) = \ln \left(\frac{\sqrt{(9-t)(1-t)}(x-t) - t(t-5) \pm x(t+3)}{\sqrt{(9-t)(1-t)}(t-x) - t(t-5) \pm x(t+3)} \right). \quad (37)$$

Diagram h_3 :

$$h_3^V(x, y) = \frac{1}{8\pi^2(x-1)^2x(2x+1)} \int_y^1 dt \left\{ \begin{aligned} & \frac{1}{1-t} \left(t^3x + t^2(4x^2 - 6x + 2) + t(-2x^3 - 29x^2 + 2) \right. \\ & \left. + x(4x^3 + 36x^2 + x - 13) \right) f_-(t, x) \\ & + \frac{t-x}{8t^2} \sqrt{\frac{9-t}{1-t}} \left(t^4x + t^3(x^2 - 4x - 4) + t^2(-2x^3 - 28x^2 + 15x + 4) \right. \\ & \left. - tx(24x^2 + 69x + 92) - 6x^3 \right) \end{aligned} \right\}, \quad (38)$$

$$\begin{aligned}
h_3^A(x, y) = & \frac{1}{8\pi^2(x-1)^2x(2x+1)} \int_y^1 dt \\
& \left\{ \frac{1}{t-1} \left(t^3x + t^2(4x^2 - 6x + 2) + t(-2x^3 - 23x^2 + 20x + 2) \right. \right. \\
& \quad \left. \left. + x(4x^3 + 24x^2 - 33x + 7) \right) f_-(t, x) \right. \\
& \quad \left. - \frac{t-x}{8t^2} \sqrt{\frac{9-t}{1-t}} \left(t^4x + t^3(x-6)x + t^2(-2x^3 - 30x^2 + 53x + 16) \right. \right. \\
& \quad \left. \left. + tx(-20x^2 - 75x + 56) + 6x^3 \right) \right\}. \tag{39}
\end{aligned}$$

Diagram h_4 :

$$\begin{aligned}
h_4^V(x, y) = & -\frac{3x}{64\pi^2(1-x)^2(2x+1)} \int_y^1 dt \sqrt{\frac{9-t}{1-t}} \\
& \left\{ -(t-x) \frac{t(2tx+t-17x-1)+23x}{6tx^2} \right. \\
& \quad \left. + \frac{t^3x+t^2(2x^2-5x+2)+t(x+2)-x(86x+13)}{3\sqrt{(9-t)(1-t)}x^2} f_-(t, x) \right. \\
& \quad \left. + \frac{1}{2}(t^3-5t^2-25t+93)g^{(0)}(t, x) + \frac{t^4-4t^3-106t^2+604t-495}{2\sqrt{(9-t)(1-t)}}g^{(1)}(t, x) \right. \\
& \quad \left. + \frac{1}{2}(-t^3+21t^2-119t+99)g^{(2)}(t, x) - \frac{1}{2}\left((9-t)(1-t)\right)^{3/2}g^{(3)}(t, x) \right\}, \tag{40}
\end{aligned}$$

$$\begin{aligned}
h_4^A(x, y) = & \frac{3x}{64\pi^2(1-x)^2(2x+1)} \int_y^1 dt \sqrt{\frac{9-t}{1-t}} \\
& \left\{ (t-x) \frac{t^2x-2t(4x+1)-7x}{3tx^2} \right. \\
& \quad \left. - \frac{t^3x+t^2(2x^2-5x+2)+t(21x+2)+(7-30x)x}{3\sqrt{(9-t)(1-t)}x^2} f_-(t, x) \right. \\
& \quad \left. - \frac{1}{2}(t-3)(t-1)^2g^{(0)}(t, x) + \frac{-t^4+4t^3+74t^2-284t+207}{2\sqrt{(9-t)(1-t)}}g^{(1)}(t, x) \right\}
\end{aligned}$$

$$+ \frac{1}{2} \left(t^3 - 21t^2 + 119t - 99 \right) g^{(2)}(t, x) + \frac{1}{2} \left((9-t)(1-t) \right)^{3/2} g^{(3)}(t, x) \right\}, \quad (41)$$

with

$$g^{(i)}(t, x) = \frac{1}{2} \int_{-1}^1 dz \frac{z^i}{\sqrt{az^2 - bz + c}} \ln \left(\frac{d - ez - k\sqrt{az^2 - bz + c}}{d - ez + k\sqrt{az^2 - bz + c}} \right) \quad (42)$$

and

$$\begin{aligned} a &= 4(9-t)(1-t)(1-x), \\ b &= 4\sqrt{(9-t)(1-t)}(x-2)(t+2x-3), \\ c &= t^2(x^2+4) - 2t(5x^2-8x+12) + 25x^2 - 48x + 36, \\ d &= -2t^2 + t((x-1)x+6) - x(x+3), \\ e &= -\sqrt{(9-t)(1-t)}(t(x-2)+x), \\ k &= t-x. \end{aligned} \quad (43)$$

Diagram h_5 :

$$\begin{aligned} h_5(x, y) &= \frac{3x}{1024\pi^2(1-x)^2(2x+1)} \int_y^1 dt \sqrt{(9-t)(1-t)} \\ &\left\{ -\frac{t-x}{6t^2x^3(t^2x+t(4-6x)+x(4x-3))} \left(t^4x(8x+1) + t^3(7x^2+39x+4) \right. \right. \\ &\quad \left. \left. + t^2(-32x^3+53x^2+11x+84) + tx(28x^2+13x-27) + 3x^2(4x-3) \right) \right. \\ &\quad \left. + \frac{4((t-9)x^2+(t-11)x-6)}{3x^3\sqrt{(9-t)(1-t)}} f_-(t, x) + \frac{4(t+3)}{x} g^{(0)}(t, x) \right. \\ &\quad \left. - \frac{4\sqrt{(9-t)(1-t)}}{x} g^{(1)}(t, x) - 4x(t^2-8t+15) j^{(0)}(t, x) \right. \\ &\quad \left. - 8x(t-4)\sqrt{(9-t)(1-t)} j^{(1)}(t, x) - 4x(9-t)(1-t) j^{(2)}(t, x) \right. \\ &\quad \left. + 8 \frac{t^2x+t(2-4x)-x-6}{x} \tilde{j}^{(0)}(t, x) + 8\sqrt{(9-t)(1-t)} \frac{tx+2}{x} \tilde{j}^{(1)}(t, x) \right\}, \end{aligned} \quad (44)$$

with

$$j^{(i)}(t, x) = \left(1 - \frac{x}{t} \right) \int_{-1}^1 dz z^i \frac{(c_3d_1 + c_1d_3)(c_2^2 + 8c_1c_3) - 6c_1c_2c_3d_2}{2c_1c_3(c_2^2 - 4c_1c_3)^2}$$

$$+ \int_{-1}^1 dz z^i \frac{(c_2^2 + 2c_1c_3)d_2 - 3c_2(c_1d_3 + c_3d_1)}{(c_2^2 - 4c_1c_3)^2 \sqrt{az^2 - bz + c}} \ln \left(\frac{d - ez - k\sqrt{az^2 - bz + c}}{d - ez + k\sqrt{az^2 - bz + c}} \right), \quad (45)$$

$$\begin{aligned} \tilde{j}^{(i)}(t, x) = & - \left(1 - \frac{x}{t}\right) \int_{-1}^1 dz z^i \frac{2c_1\tilde{d}_3 - c_2\tilde{d}_2}{c_1(c_2^2 - 4c_1c_3)} \\ & - \int_{-1}^1 dz z^i \frac{2c_3\tilde{d}_2 - c_2\tilde{d}_3}{c_2^2 - 4c_1c_3} \frac{1}{\sqrt{az^2 - bz + c}} \ln \left(\frac{d - ez - k\sqrt{az^2 - bz + c}}{d - ez + k\sqrt{az^2 - bz + c}} \right), \quad (46) \end{aligned}$$

and

$$\begin{aligned} c_1 &= \frac{x((t-6)t + 4x-3)}{t} + 4, \\ c_2 &= \frac{4\tilde{z}(t(x-2) + x) - t^2(x-4) - tx(x+3) + x^2}{t}, \\ c_3 &= \frac{x(2\tilde{z} - t)(2\tilde{z} - x)}{t}, \\ \tilde{z} &= \frac{1}{4} \left(-\sqrt{(9-t)(1-t)} z + t + 3 \right), \\ d_1 &= \frac{(t-7)(t-3)t^2 + (t(t+2) + 9)x^2 + (t(t+2) - 27)tx}{t^2}, \\ d_2 &= \frac{4\tilde{z}((t-3)t^2 + (t+3)x^2 + (t-3)tx) - t(t^2(3x+4) + tx(3x-23) + 13x^2)}{t^2}, \\ d_3 &= \frac{4\tilde{z}^2(t^2 + tx + x^2) - 6\tilde{z}tx(t+x) + 3t^2x^2}{t^2}, \\ \tilde{d}_2 &= -\frac{t(t+x-5) + 3x}{2t}, \quad \tilde{d}_3 = x - \frac{\tilde{z}(t+x)}{t}. \end{aligned} \quad (47)$$

Diagram h_6 :

$$\begin{aligned} h_6(x, y) = & -\frac{1}{128\pi^2(x-1)^2x^2(2x+1)} \int_y^1 dt \sqrt{(9-t)(1-t)} \\ & \left\{ \frac{t-x}{t^2(t^2x + t(4-6x) + x(4x-3))} \left(t^4x(6x^2 + 7x + 1) \right. \right. \\ & + t^3(-21x^3 + 9x^2 + 35x + 4) + t^2(-40x^4 - 224x^3 + 36x^2 - 21x + 84) \\ & \left. \left. + tx(60x^3 - 33x^2 + 25x - 27) + 3x^2(4x-3) \right) \right\} \end{aligned}$$

$$\begin{aligned}
& + \frac{2((t^2 - 8t + 19)x^2 + 2(t+1)x^3 - 2(t-17)x + 24)}{\sqrt{(9-t)(1-t)}} f_-(t, x) \\
& - 6(t+3)x^2(3x+2) g^{(0)}(t, x) + 6\sqrt{(9-t)(1-t)} x^2((t+6)x+2) g^{(1)}(t, x) \\
& - 6(9-t)(1-t)x^3 g^{(2)}(t, x) \\
& - 6x^2(t^2x(x+4) - 2t(5x^2 + 8x - 4) + 33x^2 + 20x - 24) \tilde{j}^{(0)}(t, x) \\
& + 12\sqrt{(9-t)(1-t)} x^2(-2(t-2)x + 7x^2 - 4) \tilde{j}^{(1)}(t, x) \\
& - 6(9-t)(1-t)x^4 \tilde{j}^{(2)}(t, x) \Big\}. \tag{48}
\end{aligned}$$

Diagram h_7 :

$$\begin{aligned}
h_7(x, y) = & \frac{3x}{64\pi^2(1-x)^2(2x+1)} \int_y^1 dt \frac{\sqrt{(9-t)(1-t)}}{5-t} \\
& \left\{ -\frac{(t-5)(t-x)(2tx+t-15x)}{6tx^2} \right. \\
& + \frac{t^3x - t^2(2x^2 + 9x - 2) + 3t(8x^2 + 3x - 2) + x(16x^2 - 18x - 17)}{3\sqrt{(9-t)(1-t)}x^2} f_-(t, x) \\
& - \frac{4(t^2x^2 + t(-8x^2 + x - 1) + (-4x^2 + 2x + 13)x)}{3\sqrt{(9-t)(1-t)}x^2} f_+(t, x) \\
& - \frac{1}{2}(-t^3 + t^2(2x + 13) - 5t(4x + 3) + 66x - 45) g^{(0)}(t, x) \\
& + \frac{1}{2}\sqrt{(9-t)(1-t)} ((t-2)t + 28x - 39) g^{(1)}(t, x) \\
& - \frac{1}{2}(9-t)(1-t)(t + 2x - 11) g^{(2)}(t, x) - \frac{1}{2}((9-t)(1-t))^{3/2} g^{(3)}(t, x) \\
& - \frac{1}{2}(t^3 - t^2(2x + 7) + t(20x + 3) - 66x - 45) \tilde{g}^{(0)}(t, x) \\
& + \frac{1}{2}\sqrt{(9-t)(1-t)} (t(t+4) - 7(4x+3)) \tilde{g}^{(1)}(t, x) \\
& \left. - \frac{1}{2}(9-t)(1-t)(t - 2x + 1) \tilde{g}^{(2)}(t, x) + \frac{1}{2}((9-t)(1-t))^{3/2} \tilde{g}^{(3)}(t, x) \right\}, \tag{49}
\end{aligned}$$

with

$$\tilde{g}^{(i)}(t, x) = -\frac{1}{2} \int_{-1}^1 dz \frac{z^i}{\sqrt{-\tilde{a}z^2 - \tilde{b}z + \tilde{c}}} \ln \left(\frac{\tilde{d} - \tilde{e}z - k\sqrt{-\tilde{a}z^2 - \tilde{b}z + \tilde{c}}}{\tilde{d} - \tilde{e}z + k\sqrt{-\tilde{a}z^2 - \tilde{b}z + \tilde{c}}} \right) \quad (50)$$

and

$$\begin{aligned} \tilde{a} &= -\frac{1}{4}(9-t)(1-t)(t^2 - 2t - 16x + 1), \\ \tilde{b} &= \frac{1}{2}\sqrt{(9-t)(1-t)}((t-6)t - 8x - 3)(t - 2x - 1), \\ \tilde{c} &= \frac{t^4 - 4t^3(x+3) + t^2(4x^2 + 44x + 30) - 4t(10x^2 + 35x - 9) + 100x^2 + 228x + 9}{4}, \\ \tilde{d} &= \frac{1}{2}(-t^3 + 3t^2(x+2) + t(-2x^2 - 16x + 3) + x(2x + 21)), \\ \tilde{e} &= \frac{1}{2}\sqrt{(9-t)(1-t)}(t(-t + x + 1) + 7x). \end{aligned} \quad (51)$$

Diagram h_8 :

$$\begin{aligned} h_8(x, y) &= \frac{1}{4\pi^2(x-1)^2(2x+1)} \int_y^1 dt \left\{ (2tx + t - 2x - 9) f_+(t, x) \right. \\ &\quad + \frac{(t-x)\sqrt{(9-t)(1-t)}}{16t^2(t(1-x) + x(x+3))} \left(t^4(1-x) - t^3(x-5) + t^2(3x^3 + 49x^2 + 44x - 72) \right. \\ &\quad \left. \left. - tx(2x^3 + 23x^2 + 107x + 144) + 6x^2(x^2 + 7x + 12) \right) \right\}. \end{aligned} \quad (52)$$

Diagram h_9 :

$$\begin{aligned} h_9(x, y) &= \frac{1}{8\pi^2(x-1)^2x(2x+1)} \int_y^1 dt \\ &\quad \left\{ \frac{2(t(2x^3 + 7x^2 - 7x + 2) - x(2x^3 + 23x^2 + 25x + 6))}{t-5} f_+(t, x) \right. \\ &\quad + \frac{1}{t-5} \left(t^3x - 2t^2(2x^2 + 5x - 1) + t(-2x^3 + 19x^2 + 12x - 6) \right. \\ &\quad \left. \left. - x(4x^3 + 16x^2 - 25x + 17) \right) f_-(t, x) \right\} \end{aligned}$$

$$\begin{aligned}
& + \frac{(t-x)\sqrt{(9-t)(1-t)}}{8t^2} \left(t^3x + t^2(x^2 - 3x - 4) + tx(-2x^2 + 5x + 20) \right. \\
& \left. + 6x^2(x+4) \right) \Big\}. \tag{53}
\end{aligned}$$

Diagram h_{10} :

$$\begin{aligned}
h_{10}(x, y) = & \frac{1}{4\pi^2(x-1)^2x^2(2x+1)} \int_y^1 dt \\
& \left\{ - \left((-t^2 + 7t - 3)x^2 + (4t + 11)x^3 + 6x^4 - 12x - 12 \right) f_-(t, x) \right. \\
& + \frac{(t-x)\sqrt{(9-t)(1-t)}}{16t^2(t^2x + t(4-6x) + x(4x-3))} \left(t^5x^3 + t^4x(x^3 + 47x^2 + 28x + 4) \right. \\
& + t^3(-2x^5 + 19x^4 - 221x^3 + 64x^2 + 124x + 16) \\
& + t^2(86x^5 + 259x^4 - 683x^3 + 12x^2 - 212x + 336) \\
& + tx(-8x^5 + 54x^4 + 201x^3 - 208x^2 + 148x - 108) \\
& \left. \left. + 6x^2(4x^4 + 13x^3 - 12x^2 + 8x - 6) \right) \right\}. \tag{54}
\end{aligned}$$

References

- [1] Tevatron Electroweak Working Group, for the CDF and D0 Collaborations, arXiv:0903.2503 [hep-ex].
- [2] M. Martinez and R. Miquel, Eur. Phys. J. **C27**, 49 (2003), [hep-ph/0207315].
- [3] V. S. Fadin and V. A. Khoze, JETP Lett. **46**, 525 (1987).
- [4] V. S. Fadin and V. A. Khoze, Sov. J. Nucl. Phys. **48**, 309 (1988).
- [5] M. J. Strassler and M. E. Peskin, Phys. Rev. **D43**, 1500 (1991).
- [6] A. H. Hoang and T. Teubner, Phys. Rev. **D58**, 114023 (1998), [hep-ph/9801397].
- [7] K. Melnikov and A. Yelkhovsky, Nucl. Phys. **B528**, 59 (1998), [hep-ph/9802379].
- [8] M. Beneke, A. Signer and V. A. Smirnov, Phys. Lett. **B454**, 137 (1999), [hep-ph/9903260].
- [9] A. H. Hoang and T. Teubner, Phys. Rev. **D60**, 114027 (1999), [hep-ph/9904468].

- [10] O. I. Yakovlev, Phys. Lett. **B457**, 170 (1999), [hep-ph/9808463].
- [11] T. Nagano, A. Ota and Y. Sumino, Phys. Rev. **D60**, 114014 (1999), [hep-ph/9903498].
- [12] A. A. Penin and A. A. Pivovarov, Phys. Atom. Nucl. **64**, 275 (2001), [hep-ph/9904278].
- [13] A. H. Hoang, A. V. Manohar, I. W. Stewart and T. Teubner, Phys. Rev. Lett. **86**, 1951 (2001), [hep-ph/0011254].
- [14] A. H. Hoang, A. V. Manohar, I. W. Stewart and T. Teubner, Phys. Rev. **D65**, 014014 (2002), [hep-ph/0107144].
- [15] A. H. Hoang, Phys. Rev. D **69**, 034009 (2004), [hep-ph/0307376].
- [16] A. Pineda and A. Signer, Nucl. Phys. **B762**, 67 (2007), [hep-ph/0607239].
- [17] M. Beneke, Y. Kiyo and K. Schuller, Nucl. Phys. **B714**, 67 (2005), [hep-ph/0501289].
- [18] M. Beneke, Y. Kiyo and K. Schuller, PoS **RADCOR2007**, 051 (2007), arXiv:0801.3464 [hep-ph].
- [19] M. Beneke and Y. Kiyo, Phys. Lett. B **668**, 143 (2008), arXiv:0804.4004 [hep-ph].
- [20] P. Marquard, J. H. Piclum, D. Seidel and M. Steinhauser, Nucl. Phys. **B758**, 144 (2006), [hep-ph/0607168].
- [21] A. V. Smirnov, V. A. Smirnov and M. Steinhauser, Phys. Lett. **B668**, 293 (2008), arXiv:0809.1927 [hep-ph].
- [22] C. Anzai, Y. Kiyo and Y. Sumino, arXiv:0911.4335 [hep-ph].
- [23] A. V. Smirnov, V. A. Smirnov and M. Steinhauser, arXiv:0911.4742 [hep-ph].
- [24] N. Brambilla, A. Pineda, J. Soto and A. Vairo, Phys. Rev. **D60**, 091502 (1999), [hep-ph/9903355].
- [25] B. A. Kniehl, A. A. Penin, V. A. Smirnov and M. Steinhauser, Nucl. Phys. **B635**, 357 (2002), [hep-ph/0203166].
- [26] A. A. Penin, V. A. Smirnov and M. Steinhauser, Nucl. Phys. **B716**, 303 (2005), [hep-ph/0501042].
- [27] M. Beneke, Y. Kiyo and K. Schuller, Phys. Lett. **B658**, 222 (2008), arXiv:0705.4518 [hep-ph].

- [28] M. Beneke, Y. Kiyo and A. A. Penin, Phys. Lett. **B653**, 53 (2007), arXiv:0706.2733 [hep-ph].
- [29] M. Beneke, Nucl. Phys. Proc. Suppl. **86** (2000) 547 [hep-ph/9910534].
- [30] I. I. Y. Bigi, Y. L. Dokshitzer, V. A. Khoze, J. H. Kühn and P. M. Zerwas, Phys. Lett. B **181**, 157 (1986).
- [31] A. H. Hoang and C. J. Reisser, Phys. Rev. D **71**, 074022 (2005), [hep-ph/0412258].
- [32] M. Beneke, A. P. Chapovsky, A. Signer and G. Zanderighi, Phys. Rev. Lett. **93**, 011602 (2004), [hep-ph/0312331].
- [33] M. Beneke, A. P. Chapovsky, A. Signer and G. Zanderighi, Nucl. Phys. **B686**, 205 (2004), [hep-ph/0401002].
- [34] M. Beneke, P. Falgari, C. Schwinn, A. Signer and G. Zanderighi, Nucl. Phys. B **792**, 89 (2008), arXiv:0707.0773 [hep-ph].
- [35] S. Actis, M. Beneke, P. Falgari and C. Schwinn, Nucl. Phys. B **807**, 1 (2009), arXiv:0807.0102 [hep-ph].
- [36] A. H. Hoang, C. J. Reisser and P. Ruiz-Femenia, Nucl. Phys. Proc. Suppl. **186**, 403 (2009), arXiv:0810.2934 [hep-ph].
- [37] A. Hoang, C. Reisser and P. Ruiz-Femenia, arXiv:1002.3223 [hep-ph].
- [38] M. Beneke, in: Proceedings of the 8th International Symposium on Heavy Flavour Physics, Southampton, England, 25-29 July 1999, [hep-ph/9911490].
- [39] M. Jezabek and J. H. Kühn, Nucl. Phys. B **314**, 1 (1989).
- [40] K. Melnikov and O. I. Yakovlev, Phys. Lett. B **324**, 217 (1994), [hep-ph/9302311].
- [41] J. Alwall *et al.*, JHEP **0709**, 028 (2007), arXiv:0706.2334 [hep-ph].
- [42] M. Beneke and V. A. Smirnov, Nucl. Phys. B **522**, 321 (1998) [hep-ph/9711391].
- [43] J. A. M. Vermaseren, Comput. Phys. Commun. **83**, 45 (1994).
- [44] D. Binosi, J. Collins, C. Kaufhold and L. Theussl, Comput. Phys. Commun. **180**, 1709 (2009), arXiv:0811.4113 [hep-ph].
- [45] J. A. M. Vermaseren, [math-ph/0010025].
- [46] R. Mertig, M. Böhm and A. Denner, Comput. Phys. Commun. **64**, 345 (1991).